

Structural and functional implications of *in vivo* phase separation of membrane protein in *Escherichia coli*

Dmitrii Linnik

Department of Biochemistry, Groningen Biomolecular Sciences & Biotechnology Institute, University of Groningen, Nijenborgh 3, 9747 AG Groningen, the Netherlands

Sumayra Sultanji

Department of Biochemistry, Groningen Biomolecular Sciences & Biotechnology Institute, University of Groningen, Nijenborgh 3, 9747 AG Groningen, the Netherlands

Jan A. Stevens

Molecular Dynamics Group, Groningen Biomolecular Sciences and Biotechnology Institute, University of Groningen, Nijenborgh 7, 9747 AG Groningen, the Netherlands

Gea K. Schuurman-Wolters

Department of Biochemistry, Groningen Biomolecular Sciences & Biotechnology Institute, University of Groningen, Nijenborgh 3, 9747 AG Groningen, the Netherlands

Rinse de Boer

Molecular Immunology, Groningen Biomolecular Sciences & Biotechnology Institute, University of Groningen, Nijenborgh 7, 9747 AG Groningen, the Netherlands

Christiaan M. Punter

Department of Biochemistry, Groningen Biomolecular Sciences & Biotechnology Institute, University of Groningen, Nijenborgh 3, 9747 AG Groningen, the Netherlands

Siewert J. Marrink

Molecular Dynamics Group, Groningen Biomolecular Sciences and Biotechnology Institute, University of Groningen, Nijenborgh 7, 9747 AG Groningen, the Netherlands

Ivan Maslov

Department of Biochemistry, Groningen Biomolecular Sciences & Biotechnology Institute, University of Groningen, Nijenborgh 3, 9747 AG Groningen, the Netherlands

Bert Poolman

b.poolman@rug.nl

Department of Biochemistry, Groningen Biomolecular Sciences & Biotechnology Institute, University of Groningen, Nijenborgh 3, 9747 AG Groningen, the Netherlands <https://orcid.org/0000-0002-1455-531X>

Keywords: in vivo biomolecular condensation, phase-separation, membrane proteins, LacY, co-condensation of proteins, single-protein mobility

Posted Date: May 14th, 2025

DOI: <https://doi.org/10.21203/rs.3.rs-6571918/v1>

License:  This work is licensed under a Creative Commons Attribution 4.0 International License.
[Read Full License](#)

Additional Declarations: There is **NO** Competing Interest.

1 Structural and functional implications of *in vivo* phase separation of
2 membrane protein in *Escherichia coli*

3

4 *Dmitrii Linnik¹, Sumayra Sultanji¹, Jan A. Stevens², Gea K. Schuurman-Wolters¹, Rinse de Boer³,*
5 *Christiaan M. Punter¹, Siewert J. Marrink², Ivan Maslov¹, and Bert Poolman^{1*}*

6

7 ¹Department of Biochemistry, Groningen Biomolecular Sciences & Biotechnology Institute,
8 University of Groningen, Nijenborgh 3, 9747 AG Groningen, the Netherlands.

9 ²Molecular Dynamics Group, Groningen Biomolecular Sciences and Biotechnology Institute,
10 University of Groningen, Nijenborgh 7, 9747 AG Groningen, the Netherlands

11 ³Molecular Immunology, Groningen Biomolecular Sciences & Biotechnology Institute,
12 University of Groningen, Nijenborgh 7, 9747 AG Groningen, The Netherlands

13

14 * E.mail: b.poolman@rug.nl

15 **Keywords:** *in vivo* biomolecular condensation, phase-separation, membrane proteins, LacY,
16 co-condensation of proteins, single-protein mobility

17

18 Abstract

19 Liquid-liquid phase-separation (LLPS) controls protein activity and dynamically
20 organizes (macro)molecules in living systems without the need for membrane-bound
21 compartments. Biomolecular condensates of water-soluble proteins have extensively been
22 studied, but LLPS of membrane proteins is uncharted territory. In this work we induce *in*
23 *vivo* condensation of lactose permease (LacY), a widely-studied model monomeric inner
24 membrane protein in *Escherichia coli*, and evaluate how it affects LacY function. We fused
25 LacY with engineered, condensate-forming protein PopTag. We observe major changes in the
26 localization and mobility of LacY^{Pop}. Molecular dynamics simulations show how the PopTag
27 domain drives the condensate-like association dynamics of LacY^{Pop} through hydrophobic
28 sticker interactions. LacY^{Pop} preserves native-level transport activity and outperforms the non-
29 condensated LacY under mild hyperosmotic stress. Perturbation experiments suggest that
30 membrane curvature drives the accumulation of LacY^{Pop} at the poles of *E. coli*. Co-
31 condensation of LacY and β -galactosidase LacZ slightly reduces their activity and results in
32 remarkable cellular reorganization of the proteins. Our research shows the localization,
33 dynamics, and function of phase-separated membrane proteins in bacteria and highlights the
34 potential of LLPS for engineering complex metabolic networks *in vivo*.

35

36 Introduction

37 Phase separation of biomolecules is an emerging field of cell biology^{1,2}. Numerous
38 examples of liquid-liquid phase separation (LLPS) have been discovered in eukaryotic cells (e.g.
39 nucleoli, Cajal bodies, stress granules, U-bodies etc.³). The physico-chemical properties of
40 condensates, such as viscosity, pH, oxygen concentration and molecular composition, can
41 differ from the surrounding milieu, favoring or disfavoring certain reactions and interactions⁴.
42 The propensity of a molecule to partition in a condensate relative to the surrounding medium
43 typically also differs. Formation of biomolecular condensates of protein and/or nucleic acids
44 is governed by attractive intermolecular interactions between motifs in intrinsically
45 disordered regions (IDR), the so-called stickers-and-spacers framework, or repeats of folded
46 domains with connecting linkers⁵. The ability of a macromolecule to interact with multiple
47 partners simultaneously (multivalency) is a requirement for phase separation⁶.

48 The fraction of water-soluble proteins with IDRs is 30-40% in mammalian cells but thought
49 to be lower in bacteria³. A subfraction of these molecules enable multivalent interactions that
50 drive biomolecular condensation. Little is known of phase-separation of transmembrane
51 proteins driven by intermolecular protein interactions. Some examples are T-cell receptors in
52 mammalian cells, Rv1747 protein in *Mycobacterium tuberculosis*, and PodJ in *Caulobacter*
53 *vibrioides*. The phase separation of T-cell receptors and their auxiliary proteins plays a role in
54 the transduction of signals within the immune system⁷. The phase separation and 2D
55 clustering of the ATP-binding cassette transporter Rv1747 is promoted by condensation of two
56 2-Forkhead-associated cytosolic domains linked by an IDR and tuned by phosphorylation⁸. In
57 PodJ protein part of the cytosolic coiled-coil domain and IDR are responsible for the
58 condensate formation⁹. We note that IDRs are present in numerous types of membrane
59 proteins and often implicated in their regulation, but they are generally not seen as possibility
60 for condensation of the proteins and putative multivalency has not been explored^{10,11}. Next
61 to protein-driven phase separation, membrane proteins can be organized via scaffolding
62 proteins like flotillins^{12,13} or partition differentially in liquid-disordered and liquid-ordered lipid
63 domains in the membrane¹⁴, but these mechanisms are not relevant for this study.

64 To study the mechanisms and implications of multivalent site-specific interactions
65 between soluble regions of membrane proteins *in vivo*, we use the condensation domain
66 PopTag to drive phase separation of an integral membrane protein. PopTag is the C-terminal
67 part of the phase separating protein PopZ, which is important for the asymmetrical division of
68 *Caulobacter vibrioides*^{15,16}. PopTag consists of three sticker sequences separated by IDRs,
69 allowing multivalent interactions and thus condensate formation. We fused this protein tag
70 to the C-terminus of lactose permease LacY to drive biomolecular condensate formation of an
71 integral membrane protein that normally is homogenously distributed in the inner membrane
72 of *E. coli*.

73 Addition of PopTag to LacY results in a predominantly polar localization of the fusion
74 protein. We show the condensate-like behavior of LacY^{Pop} fused to a fluorescent protein
75 mEos3.2 (LacY^{mEos-Pop}, Table S1) by fluorescence recovery after photobleaching (FRAP),

76 photoactivated localization microscopy (PALM), and single-molecule displacement mapping
 77 (SMdM). Using coarse-grained molecular dynamics simulations, we show how the PopTag
 78 domains bridge LacY proteins through hydrophobic sticker interactions and form a dynamic
 79 network of protein-protein associations leading to condensate formation. In a series of
 80 perturbation experiments we show that nucleoid exclusion is not critical for the polar
 81 localization, while local membrane curvature plays a role. Using ¹⁴C-lactose transport
 82 experiments, we show that LacY is fully active in condensates and even outperforms native
 83 LacY. Finally, we designed and characterized heterocondensates of LacY^{Pop} with its
 84 downstream lactose-metabolizing enzyme, β -galactosidase (LacZ)-PopTag (LacZ^{Pop}).
 85

86 Results

87 **PopTag induces biomolecular condensation of LacY in the inner membrane of** 88 ***E. coli***

89 Genes for LacY-mEos3.2 and LacY-mEos3.2-PopTag fusions were inserted in the pBAD
 90 vector and transformed into *E. coli* BW25113, resulting in BW25113 LacY^{mEos} and BW25113
 91 LacY^{mEos-Pop}. Wide-field fluorescence microscopy shows that LacY^{mEos} is equally distributed in
 92 the inner membrane, without preferred localization, whereas LacY^{mEos-Pop} is predominantly
 93 present at the cell poles but discrete foci are also visible at the lateral membrane (Figure 1a).
 94 To reveal fine details of LacY^{mEos-Pop} clusters we performed PALM microscopy with live cells
 95 and cells fixed with formaldehyde-glutaraldehyde (Figure 1b). In live cells, single-molecule
 96 localizations, recorded for 30 min (~100.000 frames), show patterns akin those of the wide-
 97 field fluorescence microscopy images, whereas reconstructions recorded for 6 min (~20.000
 98 frames) reveal multiple clusters on the lateral membrane, similar to what has been seen for
 99 Rv1747 in *M. tuberculosis*⁸. The fraction of localizations at the cell poles is two times higher
 100 for LacY^{mEos-Pop} (0.62 ± 0.06) than for LacY^{mEos} (0.30 ± 0.04) (Figure 1c). In fixed cells, the
 101 localization of LacY^{mEos-Pop} is preserved, but the apparent size of the clusters is smaller,
 102 presumably due to reduction of the “motion blur” (Supplementary Video 1). Thus, LacY^{mEos-Pop}
 103 predominantly localizes at cell poles and forms mobile foci in the lateral membrane that
 104 become immobile upon fixation.

105 To investigate the mobility of LacY^{mEos} and LacY^{mEos-Pop}, we performed fluorescence
 106 recovery after photobleaching (FRAP) and single-molecule displacement mapping (SMdM¹⁸⁻
 107 ²⁰) experiments. Non-condensated LacY^{mEos} recovered with a half-time of 0.61 ± 0.14 sec and
 108 reached ~80% of the initial fluorescence (Figure 1d and S1). The fluorescence recovery of
 109 LacY^{mEos-Pop} had a half-time of 198 ± 66 sec seconds and reached ~20% of the initial
 110 fluorescence, and the majority of the molecules partition inside punctuated condensates upon
 111 recovery. The moderate recovery of LacY^{mEos-Pop} reflects protein exchange between the
 112 biomolecular condensate at the bleached pole and the lateral membrane (small fraction of
 113 total LacY^{mEos-Pop}); the fluorescence of the non-bleached pole does not change during the
 114 recovery phase.

115 Next, we examined the mobility of individual LacY^{mEos} and LacY^{mEos-PopTag} molecules with
116 SMdM²¹ (Figure 1e). The apparent diffusion coefficient (D) of LacY^{mEos} is lower at the cell poles
117 compared to the lateral membrane ($D = 0.17 \pm 0.04 \mu\text{m}^2/\text{s}$ versus $0.22 \pm 0.06 \mu\text{m}^2/\text{s}$, t-test
118 p-value = 0.0002) (Figure 1f). This decrease in D suggests a lower protein mobility at the cell
119 poles but can also be a result of two-dimensional projection of protein movement across the
120 membrane. The apparent diffusion coefficient of LacY^{mEos-Pop} is similar between the cell poles
121 and the lateral membrane ($D = 0.11 \pm 0.02 \mu\text{m}^2/\text{s}$ vs $0.12 \pm 0.01 \mu\text{m}^2/\text{s}$, t-test p-value = 0.34)
122 and is 35% lower than that of polar LacY^{mEos}. Since LacY^{mEos-Pop} mobility in the lateral
123 membrane and at the cell pole is reduced to a similar extent, we conclude that LacY^{mEos-Pop}
124 forms not only large condensates at the cell poles, but also smaller condensates in the lateral
125 membrane.

126 We performed transmission electron microscopy on cryo-fixed BW25113 LacY^{mEos} and
127 BW25113 LacY^{mEos-Pop} cells to verify the membrane localization of LacY^{mEos-Pop} condensates at
128 higher resolution than observed by light microscopy. We observe electron-dense regions on
129 the cytoplasmic face of the inner membrane at the cell pole in 4 out of 6 BW25113 LacY^{mEos-}
130 ^{Pop} cells and in 2 out of 10 BW25113 LacY^{mEos} cells (Figure 1g, Figure S2). The approximate
131 thickness of these regions is 10 nm, which is similar to the predicted length of the mEos3.2-
132 PopTag part of LacY^{mEos-Pop}. Remarkably, the shape and integrity of the inner membrane
133 adjacent to the electron-dense regions at the cell poles are preserved. These data suggest that
134 LacY^{mEos-Pop} condensates anchor to the inner membrane without deforming it. Collectively, our
135 observations suggest that LacY^{mEos-Pop} forms two-dimensional biomolecular condensates in
136 the inner membrane of *E. coli*, with large condensates at the cell poles and smaller ones in the
137 lateral membrane.

138

139

140

141

142

143

144

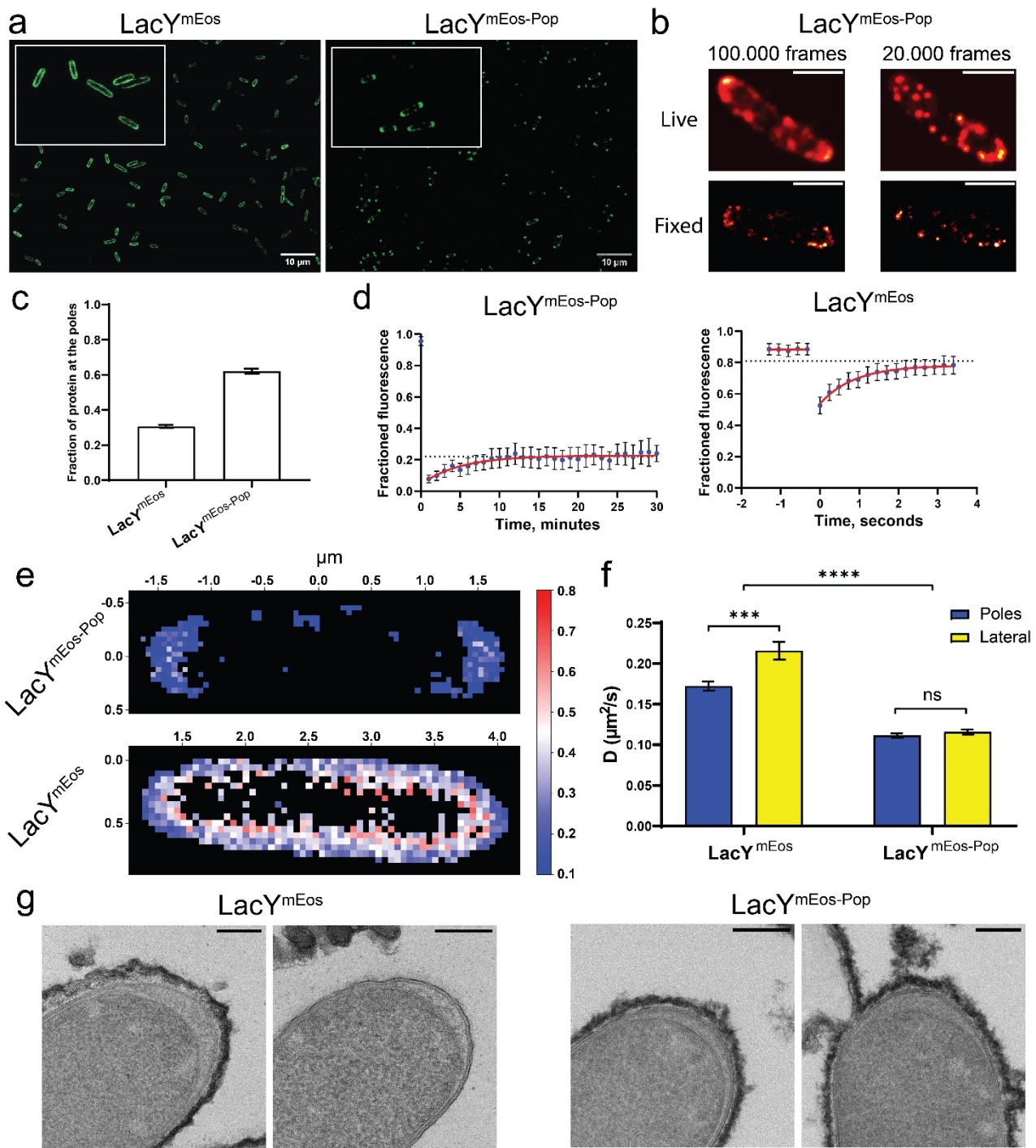
145

146

147

148

149



150
151 **Figure 1. Localization and mobility of LacY^{mEos} and LacY^{mEos-Pop} in *E. coli*.** (a) Wide-field
152 fluorescence microscopy images of LacY-mEos3.2 and LacY-mEos3.2-PopTag for localization
153 of the proteins in *E. coli* BW25113. Protein expression was induced with 0.1% w/v L-arabinose
154 for 4 h. (b) PALM reconstruction of LacY-mEos3.2-PopTag in representative live and fixed cells.
155 Left column: 100,000 frames of acquisition were used for super-resolution reconstruction;
156 right panel: 20,000 frames of the same acquisition. (c) Fraction of localizations at the cell poles
157 for BW25113 LacY^{mEos} and BW25113 LacY^{mEos-Pop} strains; the pole was taken as 20% of the total
158 cell length. Data presented and mean \pm SEM, averaged over 23 and 13 cells for BW25113
159 LacY^{mEos} and BW25113 LacY^{mEos-Pop}, respectively. (d) Fluorescence recovery profiles of cells
160 expressing LacY^{mEos} and LacY^{mEos-Pop}. A cell pole was photobleached and the intensity recovery

161 over time was measured. Data is shown as mean \pm 95% CI, n=23 for BW25113 LacY and n=21
 162 for BW25113 LacY^{Pop}. The recovery curve was fitted with the exponential plateau equation.
 163 **(e)** Diffusion maps of *E. coli* BW25113 LacY^{mEos} (up) and BW25113 LacY^{mEos-Pop} (bottom). The
 164 pixel bin size of the diffusion maps was 100 nm. Diffusion maps were reconstructed by fitting
 165 displacements starting in each pixel bin with equation 3. **(f)** Apparent diffusion coefficients of
 166 LacY^{mEos} and LacY^{mEos-Pop} measured at the cell poles (determined as 20% of cell length) and
 167 lateral membrane at mid-cell. 23 and 21 cells were measured for BW25113 LacY^{mEos} and
 168 BW25113 LacY^{mEos-Pop} strains, respectively, and data are presented as mean \pm SEM. **(g)**
 169 Transmission electron microscopy images of 100 nm thin sections of *E. coli* BW25113 LacY^{mEos}
 170 and BW25113 LacY^{mEos-Pop}. Significance levels are presented as asterisk signs: (ns) for p>0.05,
 171 (*) for p<0.05 and (****) for p<0.0001.

172

173 **Hydrophobic stickers drive LacY^{Pop} condensation**

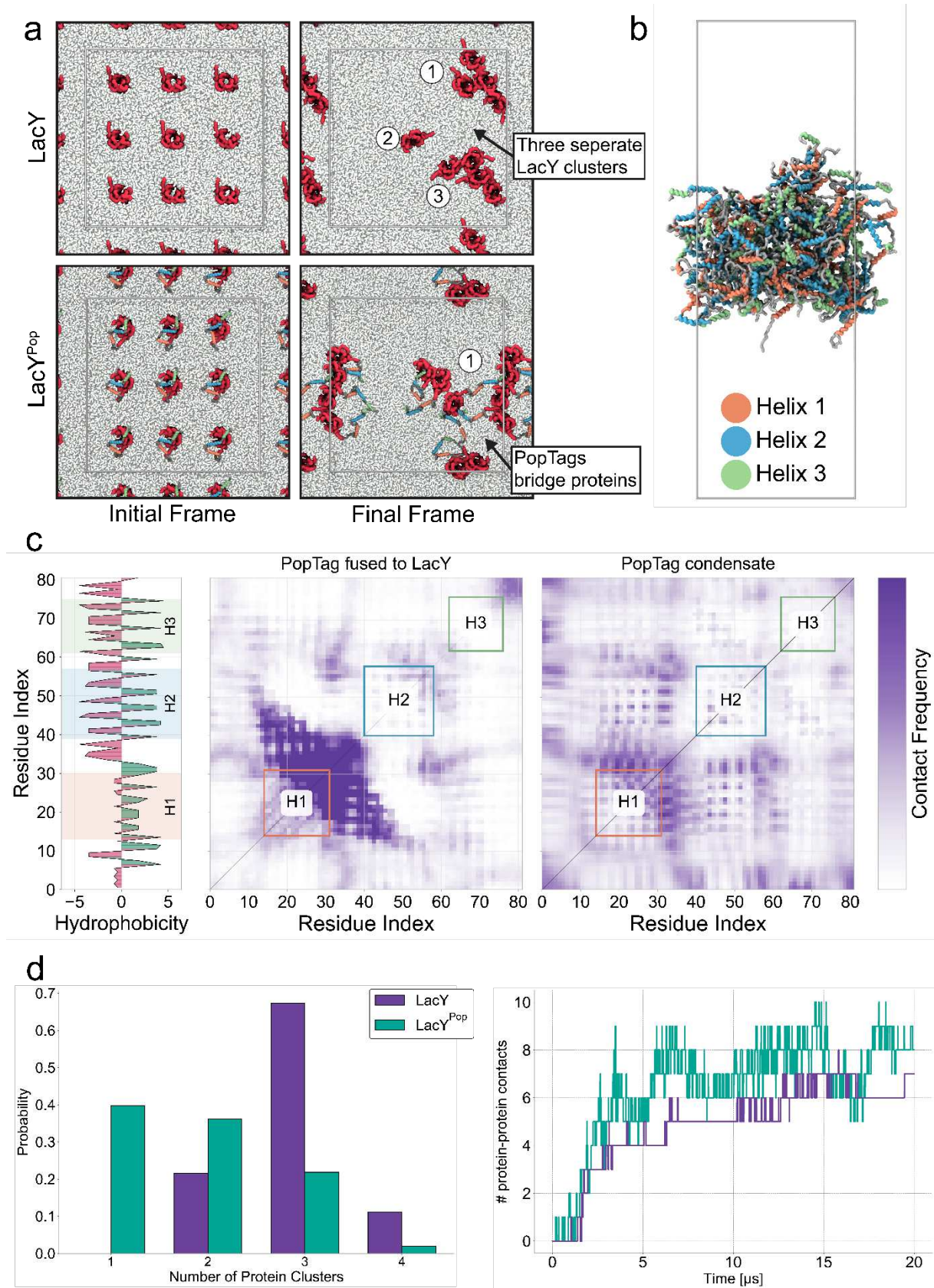
174 To investigate how the fused PopTag influences the organization of LacY in the
 175 membrane, we performed coarse-grained molecular dynamics (MD) simulations of nine LacY
 176 proteins in an *E. coli*-like lipid membrane, with and without a PopTag (Figure 2a). The
 177 simulations were executed in triplicate for better statistics on our observations. The proteins
 178 were initially positioned in equally spaced grid configurations. During a 20 μ s simulation, both
 179 proteins show a clear difference in clustering behavior. LacY proteins without a PopTag formed
 180 relatively static small clusters, maintaining approximately three separate clusters throughout
 181 the simulation. In contrast, LacY^{Pop} proteins show substantially more dynamic interactions,
 182 ultimately even forming a single large cluster during the simulations. Quantitative analysis
 183 confirms this difference in clustering dynamics (Figure 2d and S3), with LacY^{Pop} having more
 184 fluctuations in the number of protein-protein interactions.

185 To understand the molecular mechanism behind the PopTag-mediated clustering, we
 186 analyzed the specific residue contacts involved in PopTag-PopTag interactions. First, we
 187 performed simulations of the PopTag alone (Figure 2b). The contact map analysis reveals that
 188 inter-PopTag interactions in condensates are primarily driven by helix 1 (residues 14-31) and
 189 to a lesser extent by helix 2 (residues 40-58) (Figure 2c, right panel). We then compared these
 190 results to the contacts formed by PopTag when fused to LacY in the membrane simulations
 191 described above. This comparison shows the same interaction motif in both contexts, with
 192 helix 1 being the primary driver of inter-PopTag interactions (Figure 2c, left panel). The
 193 interaction interface in both cases is dominated by the amphipathic α -helices with high
 194 hydrophobic moment. The hydrophobic faces of these putative helices most likely form the
 195 "stickers" for condensation, as indicated by the hydrophobicity profile along the residue index.
 196 This suggests that the hydrophobic character of the PopTag is important for its self-association
 197 properties.

198 In our MD simulations, the PopTag helices embed at the membrane surface due to
 199 their amphipathic nature, creating membrane-mediated PopTag-PopTag interactions (Fig 2a).
 200 This membrane interaction potentially competes with the solution-mediated condensate
 201 formation, as hydrophobic residues engaged with the membrane are unavailable for PopTag-
 202 PopTag interactions. It is feasible that a dynamic equilibrium exists between membrane-
 203 mediated and solution-mediated condensate formation. To explore this, we performed

204 additional simulations of LacY^{Pop} where proteins were configured at high concentration with
205 the PopTags extended into the solvent (Figure S4). This indeed reduced membrane association
206 and allowed more extensive PopTag-PopTag interactions and network formation through
207 association of the helical parts. Furthermore, in all our simulations with LacY^{Pop}, we observed
208 larger local membrane deformations compared to the system with LacY alone (Figure S5). This
209 locally induced membrane curvature may affect the dynamics and organization of the
210 membrane protein, which represents an interesting focus for future study, and may
211 contribute a driving force for the clustering of LacY^{Pop} at the cell poles.

212 Together, our simulations demonstrate that the PopTags mediate interactions
213 between otherwise non-associating LacY proteins through their hydrophobic interfaces. This
214 creates a dynamic network of protein-protein interactions that drives the condensate-like
215 behavior of LacY^{Pop} membrane proteins.



216

217 **Figure 2. Molecular dynamics simulations show PopTag-mediated clustering of LacY**
 218 **membrane proteins. (a)** Comparison of clustering behavior between LacY (top) and LacY^{Pop}
 219 (bottom). Initial frames (left) show the start configuration of the simulation, while the end
 220 frames (right) show the final protein organization after 20 μ s. **(b)** Representative snapshot

221 from the PopTag condensate simulation, with helices colored (helix 1 in red, helix 2 in blue,
 222 helix 3 in green). **(c)** Contact map analysis comparing inter-PopTag interactions when fused to
 223 LacY (left) versus in a solution-mediated condensate (right). The hydrophobicity profile (far
 224 left) illustrates the amphipathic nature of PopTag's helices, with helix 1 (orange box) showing
 225 highest interaction frequency in both environments. **(d)** Quantitative analysis of clustering
 226 dynamics showing the probability distribution of protein cluster numbers during the last 10 μ s
 227 of simulations **(left)** and the time evolution of protein-protein contacts throughout a
 228 representative 20 μ s trajectory **(right)** for LacY^{Pop} (teal) and LacY (purple).

229

230 Membrane curvature impacts distribution of LacY condensates

231 What determines the predominant polar localization of phase-separated LacY-
 232 mEos3.2-PopTag? We tested whether the nucleoid would exclude the condensates from the
 233 lateral membrane. We imaged BW25113 LacY^{mEos} and BW25113 LacY^{mEos-Pop} cells after
 234 treatment with cephalexin for four and seven hours (Figure 3ab). Cephalexin leads to
 235 elongation of *E. coli* and accumulation of multiple nucleoids in one cell²². After 4-hour
 236 cephalexin treatment we observed cells with two nucleoids per cell, using DAPI as a DNA-
 237 staining dye. LacY^{mEos} is homogeneously distributed in the membrane, while LacY^{mEos-Pop} has
 238 the same distribution as in untreated cells: the majority of the condensates are at the cell
 239 poles but some smaller foci are found at the lateral membrane. After 7-hour cephalexin
 240 treatment, the number of nucleoids per cell increased, but for both LacY variants the
 241 localization patterns remain, with the majority of LacY^{mEos-Pop} at the poles and LacY^{mEos}
 242 homogeneously distributed. Importantly, we do not observe accumulation of LacY^{mEos-Pop} in the
 243 inter-nucleoid regions, suggesting that LacY^{mEos-Pop} localization is not governed by nucleoid
 244 exclusion.

245 To further investigate the role of the nucleoid in LacY^{mEos-Pop} positioning, we visualized
 246 LacY^{mEos-Pop} in nucleoid-free *E. coli* LY177 cells, where arabinose-induced expression of *I-SceI*
 247 endonuclease leads to nucleoid degradation²³, which was confirmed by DAPI staining (Figure
 248 3c). Upon nucleoid degradation, LacY^{mEos-Pop} is mostly in the polar regions with some foci on
 249 the lateral membrane, while LacY^{mEos} remains homogeneously distributed over the membrane.
 250 These experiments rule out that nucleoid exclusion causes polar location of the LacY^{mEos-Pop}
 251 membrane condensates.

252 Next, we evaluated the effect of membrane curvature on the localization of the
 253 proteins, using spheroplasts prepared from BW25113 LacY^{mEos} and BW25113 LacY^{mEos-Pop} cells
 254 (3d)^{24,25}. Spheroplasts made from BW25113 LacY^{mEos} served as control and show homogenous
 255 LacY^{mEos} distribution. Spheroplasts from BW25113 LacY^{mEos-Pop} show a variety of LacY-
 256 mEos3.2-PopTag distributions, ranging from multiple clusters per spheroplasts to almost
 257 homogeneous protein distribution. We then measured the same cells 30 min after
 258 spheroplasts formation and find a dissolution of LacY^{mEos-Pop} condensates from the original
 259 poles, and the cell shape change is associated with a more homogenous localization pattern.
 260 To capture the redistribution of LacY^{mEos-Pop} upon spheroplast formation over time, we
 261 immobilized *E. coli* cells with agarose pads, supplemented with the “cocktail” for spheroplasts

262 formation to trigger the shape change. The time-lapse videos clearly show the gradual
263 redistribution of large phase-separated condensates from distinct foci to homogeneously
264 localized protein over approximately 40 min (Supplementary Video 2). Thus, the loss of pole
265 localization of phase-separated membrane-bound condensates coincides with the loss of the
266 pole curvature. To reintroduce curvature in spheroplasts with homogeneously distributed
267 LacY^{mEos-Pop}, we induced plasmolysis in the spheroplasts immobilized under agarose pads
268 supplemented with 0.5 M NaCl. The LacY^{mEos-Pop} distribution was monitored by wide-field
269 fluorescence microscopy (Figure 3e). Remarkably, upon plasmolysis, LacY^{mEos-Pop} condensates
270 are no longer homogeneously distributed in the spheroplasts but predominantly localize at
271 highly curved, concave membrane regions. These observations highlight the importance of
272 membrane curvature in the spatial distribution of LacY^{mEos-Pop}.

273

274

275

276

277

278

279

280

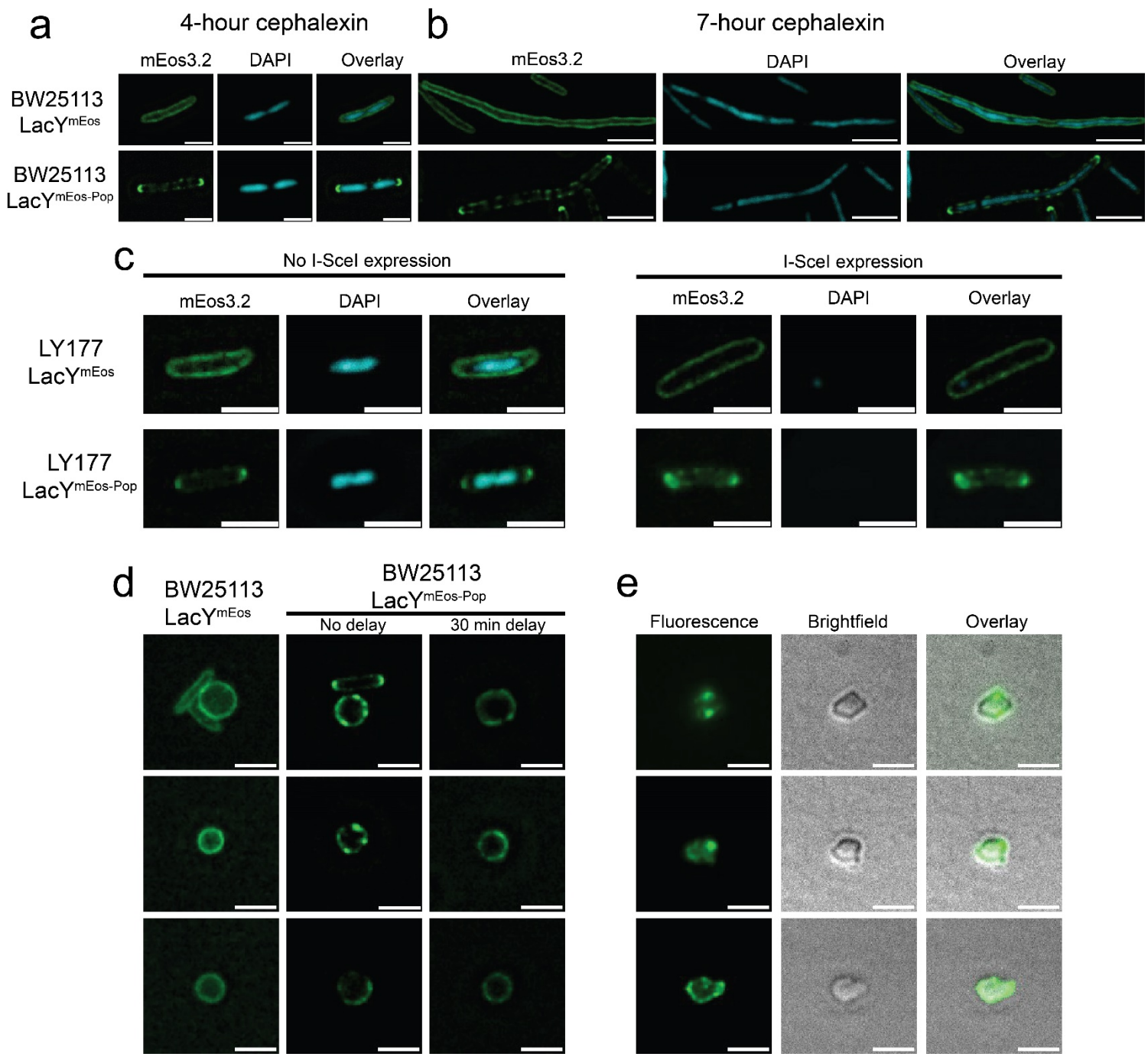
281

282

283

284

285



286

287 **Figure 3. Perturbation of nucleoid and shape of *E. coli* reveals curvature-dependent LacY^{mEos}-
288 Pop distribution.** (a) and (b) Wide-field fluorescence microscopy images of *E. coli* BW25113
289 LacY^{mEos} and BW25113 LacY^{mEos-Pop}, treated with cephalixin for (a) 4 h and (b) 7 h.
290 Homogeneous distribution of LacY-mEos3.2 and predominantly polar localization of LacY-
291 mEos3.2-PopTag is observed in all conditions. To visualize the nucleoid, cells were stained with
292 15 μ M DAPI before the acquisition. Scale bars are 3 μ m for 4-hour treated and 5 μ m for 7-hour
293 treated cells. (c) Wide-field fluorescence microscopy images of *E. coli* LY177 LacY^{mEos} and
294 LY177 LacY^{mEos-Pop}. Left panel: cells not producing the *I-SceI* endonuclease. Right panel: cells
295 producing *I-SceI* endonuclease. Degradation of nucleoid was confirmed by DAPI staining. The
296 brightness of the mEos3.2 and DAPI channels was adjusted to the same levels for left and right
297 panels. Scale bars are 3 μ m. (d) Wide-field fluorescence microscopy images of spheroplasts

298 formed from *E. coli* BW25113 LacY^{mEos} and BW25113 LacY^{mEos-Pop}. BW25113 LacY^{mEos-Pop} cells
 299 were measured immediately after spheroplast formation and after 30 min incubation at room
 300 temperature. Scale bars are 3 μ m. The dynamic redistribution of phase-separated LacY^{mEos-Pop}
 301 over approximately 30 min can be seen in Video 1. **(e)** Wide-field fluorescence microscopy
 302 images of LacY^{mEos-Pop} distribution in hyperosmotically stressed spheroplasts after 30 min of
 303 incubation with 0.5 M NaCl. LacY-mEos3.2-PopTag is no longer homogeneously distributed
 304 and forms clusters at membrane regions with curvature. Scale bars are 3 μ m.

305

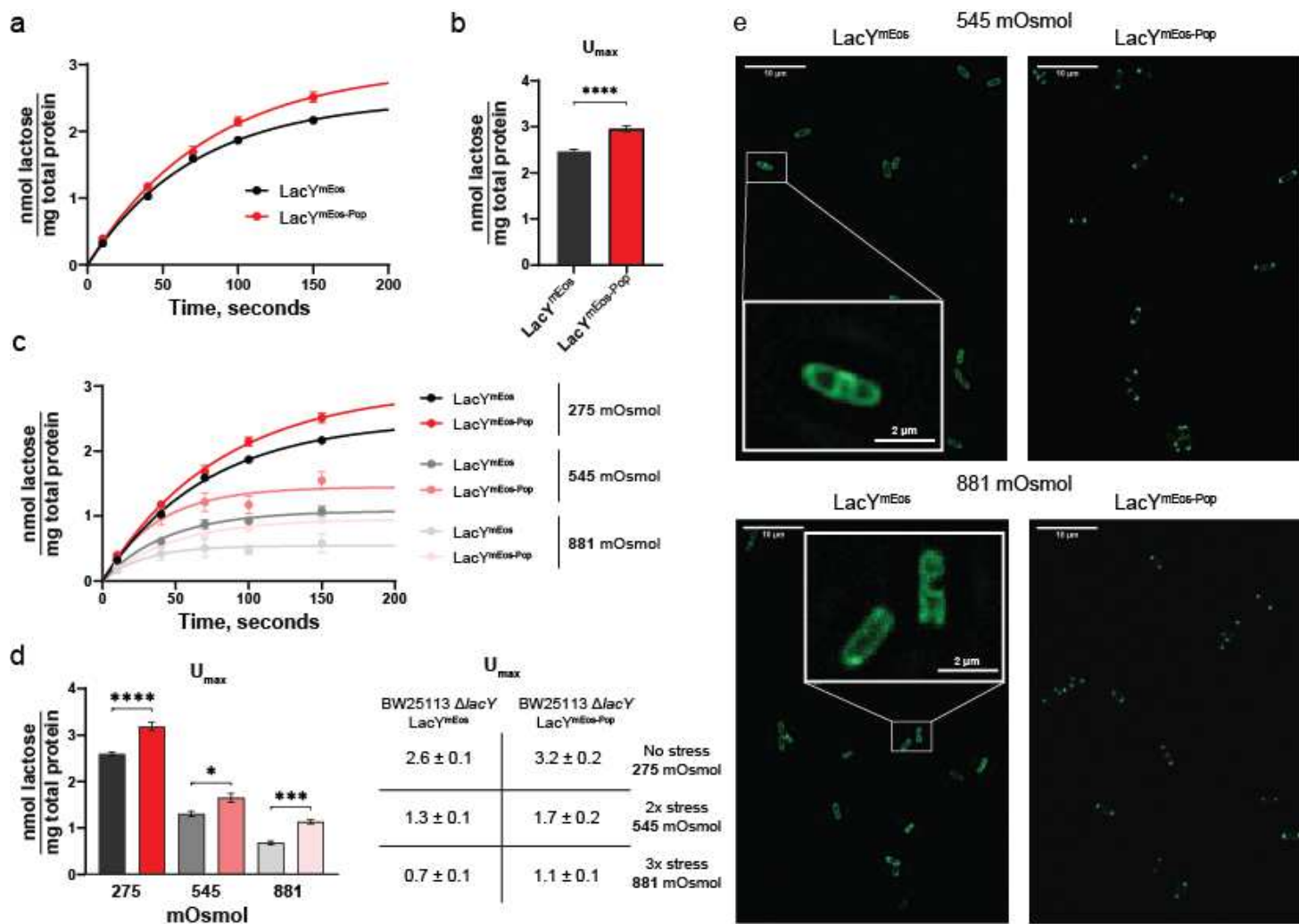
306 **Activity of condensated LacY**

307 To evaluate the effect of condensation on LacY transport activity, we used ¹⁴C-lactose
 308 and determined the uptake of the substrate by LacY^{mEos} and LacY^{mEos-Pop} in *E. coli* BW25113
 309 Δ lacY (Figure 4a). The cells producing LacY^{mEos-Pop} import slightly more lactose compared to
 310 the cells with LacY^{mEos}, which is seen as higher plateauing levels of the uptake curves ($U_{MAX} =$
 311 2.96 ± 0.17 versus 2.48 ± 0.10 nmol lactose/mg total cell protein, *t*-test *p*-value < 0.0001,
 312 Figure 4b). The expression of the LacY variants was similar as determined by fluorescence
 313 analysis of cell lysates separated by SDS-PAGE (Figure S6).

314 Further, we tested whether LacY condensation can rescue the decrease of activity
 315 under stress conditions, i.e. hyperosmotic stress²⁶. We measured ¹⁴C-lactose uptake of cells
 316 without stress and upon an increase of NaCl concentration of 160 mM or 320 mM, resulting
 317 in 2- or 3-fold increase in osmolarity (Figure 4c). Under the higher osmolarity, the maximum
 318 levels of lactose uptake U_{MAX} reduce both for BW25113 Δ lacY LacY^{mEos} and BW25113 Δ lacY
 319 LacY^{mEos-Pop} cells (Figure 4d). Remarkably, under all measured conditions, LacY^{mEos-Pop}
 320 outperforms LacY^{mEos}.

321 We then visualized the protein distribution in osmotically stressed BW25113 Δ lacY
 322 LacY^{mEos} and BW25113 Δ lacY LacY^{mEos-Pop} cells (Figure 4e). Both strains show membrane
 323 deformations indicative of plasmolysis, and the effects are more pronounced with the 3-fold
 324 than with the 2-fold osmolarity increase. However, we find fewer deformed BW25113 Δ lacY
 325 LacY^{mEos-Pop} cells than BW25113 Δ lacY LacY^{mEos}; 24 ± 7 % versus 53 ± 8 % at 3-fold osmolarity
 326 increase (number of analyzed fields of view is 5, *t*-test *p*-value = 0.0003), which suggests that
 327 membrane-bound biomolecular condensates protect cells against osmotic deformation. A
 328 smaller degree of plasmolysis will diminish the volume decrease, and this may explain the
 329 higher U_{MAX} of LacY^{mEos-Pop} expressing cells.

330



331

332 **Figure 4. LacY activity outside and inside biomolecular condensates** (a) ^{14}C -lactose uptake by
 333 $E. coli$ BW25113 $\Delta lacY$ LacY^{mEos} and BW25113 $\Delta lacY$ LacY^{mEos-Pop}. Data were fitted with an
 334 exponential plateau equation and U_{MAX} is the plateau value of the fit. R^2 for the fits of
 335 BW25113 $\Delta lacY$ LacY^{mEos} and BW25113 $\Delta lacY$ LacY^{mEos-Pop}, are 0.97 and 0.95, respectively. Data
 336 are presented as mean \pm SEM, $n = 7$. (b) Box plots of U_{MAX} of ^{14}C -lactose uptake by BW25113
 337 $\Delta lacY$ LacY^{mEos} and BW25113 $\Delta lacY$ LacY^{mEos-Pop}. Data are presented as mean \pm SEM, $n = 7$. (c)
 338 ^{14}C -lactose uptake curves of BW25113 $\Delta lacY$ LacY^{mEos} and BW25113 $\Delta lacY$ LacY^{mEos-Pop} cells
 339 after osmotic upshift. Cells grown in 275 mOsmol were upshifted with 160 mM NaCl or 320
 340 mM NaCl, resulting in medium osmolarities of 545 and 881 mOsmol, respectively. Data are
 341 presented as mean \pm SEM, $n = 7$ for 275 mOsmol and 4 for 545 and 881 mOsmol. (d) Left panel
 342 – box plots of U_{MAX} of ^{14}C -lactose uptake by $E. coli$ BW25113 $\Delta lacY$ LacY^{mEos} and BW25113 $\Delta lacY$
 343 LacY^{mEos-Pop} after osmotic upshift. Data are presented as mean \pm SEM, $n = 7$ for 275 mOsmol
 344 and 4 for 545 and 881 mOsmol conditions. Right panel – table of U_{MAX} parameters for all
 345 measured conditions. (e) Wide-field fluorescence microscopy images of $E. coli$ BW25113 $\Delta lacY$
 346 LacY^{mEos} and BW25113 $\Delta lacY$ LacY^{mEos-Pop} after osmotic upshift from 275 to 545 and 881
 347 mOsmol. 5-times zoom-ins show severely deformed $E. coli$ BW25113 $\Delta lacY$ LacY. Significance
 348 levels are presented as asterisk signs: (ns) for $p > 0.05$, (*) for $p < 0.05$, (**) for $p < 0.0001$ and
 349 (****) for $p < 0.0001$.

350 **PopTag is driving the co-condensation of LacY and LacZ *in vivo***

351 Heterocondensation of cytoplasmic and membrane proteins has to the best of our
 352 knowledge not been explored but could potentially speed up reaction networks by direct pass
 353 on of substrates from transporter to enzyme. Hence, we co-expressed LacY and LacZ fusions
 354 with mEos3.2 and mRuby fluorescent proteins, respectively, with and without C-terminal
 355 PopTag (Table 1). We visualized the localization of membrane (LacY) and cytoplasmic (LacZ)
 356 protein for all combinations with and without PopTag by confocal laser-scanning fluorescence
 357 microscopy (Figure 5a).

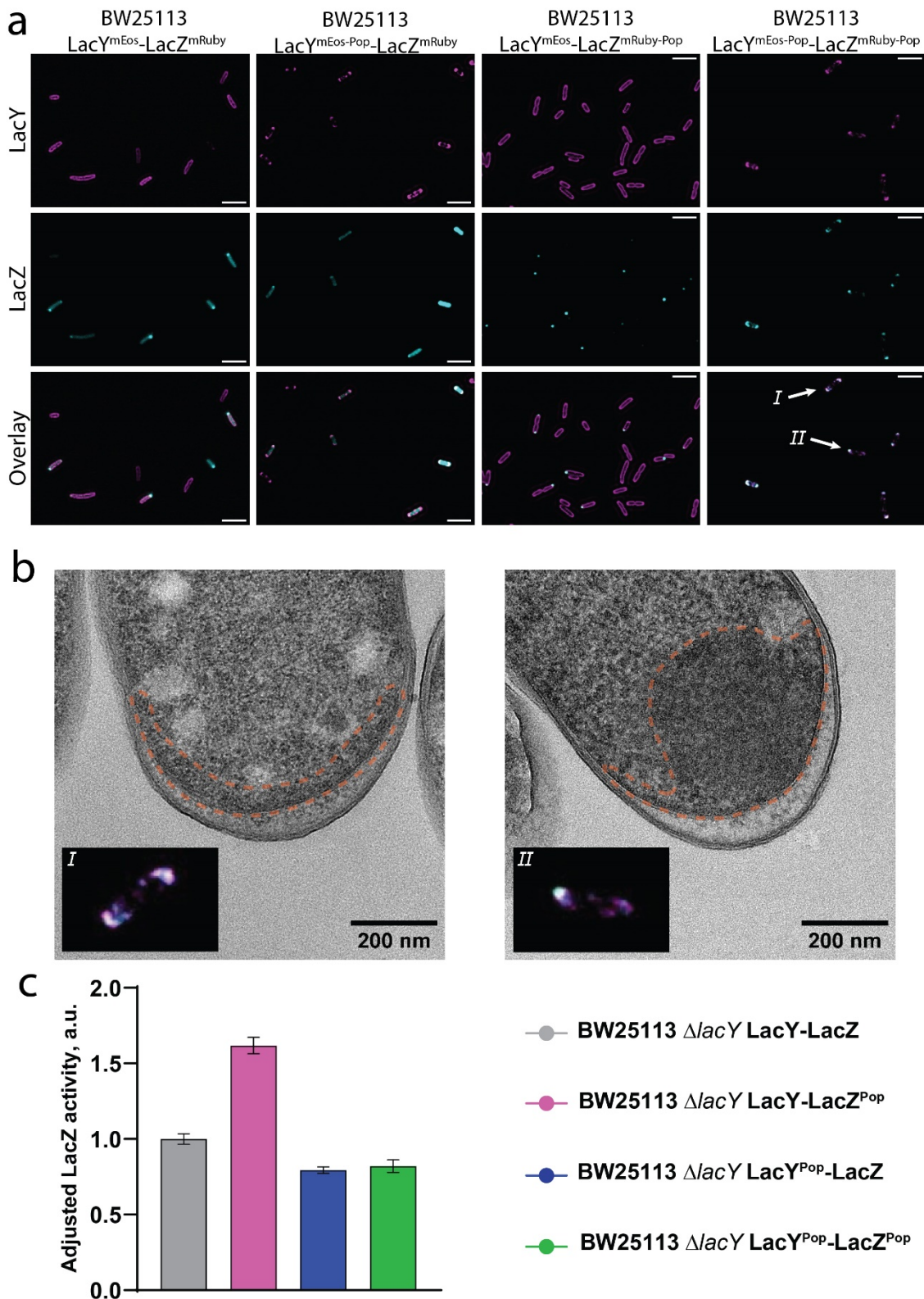
358 LacY^{mEos} distributed homogeneously across the membrane and LacY^{mEos-Pop} was
 359 predominantly present at the cell poles with smaller clusters in the lateral membrane,
 360 independent of co-expression of either LacZ^{mRuby} or LacZ^{mRuby-Pop}. LacZ^{mRuby} distributed mostly
 361 homogeneously in the cytoplasm, independent of co-expression of LacY^{mEos} or LacY^{mEos-Pop};
 362 some inclusion bodies are visible at the cell poles, which is expected as β -galactosidase fusions
 363 are prone to aggregation^{27,28}, even at low inducer concentration (0.000001% w/v L-rhamnose)
 364 and 30 °C in minimal media. Remarkably, LacZ^{mRuby-Pop} is localized differently in cells producing
 365 LacY^{mEos} and LacY^{mEos-Pop}. In BW25113 LacY^{mEos}-LacZ^{mRuby-Pop} cells, LacZ^{mRuby-Pop} forms spherical
 366 condensates at the cell poles, while in BW25113 LacY^{mEos-Pop}-LacZ^{mRuby-Pop} cells we observe two
 367 different morphologies (Figure 5a). In the first, more frequent, scenario, LacZ^{mRuby-Pop} forms
 368 large dome-shaped condensates at the cell poles and smaller condensates in the lateral
 369 membrane colocalizing with LacY^{mEos-Pop}. In the second, less frequent, scenario, LacZ^{mRuby-Pop}
 370 forms spherical condensates at the cell poles without smaller condensates in the lateral
 371 membrane. We hypothesize that in scenario I LacZ^{mRuby-Pop} fully covers the in-membrane
 372 condensate of LacY^{mEos-Pop}, and in scenario II, large cytosolic condensates of LacZ^{mRuby-Pop} only
 373 partially interact with in-membrane condensates of LacY^{mEos-Pop}.

374 Transmission electron microscopy of BW25113 LacY^{mEos-Pop}-LacZ^{mRuby-Pop} also shows
 375 two scenarios of heterocondensate formation (Figure 5b, Figure S7). Scenario I was observed
 376 in 5 out of 15 cell sections and shows the electron-dense region at the cytoplasmic face of the
 377 inner membrane, and it is thicker (~50 nm) than that of BW25113 LacY^{mEos-Pop} cells (~10 nm,
 378 Figure 5b, left). Interestingly, in one cell, a large electron-dense region is seen in the
 379 cytoplasm, which is partially in contact with a thin (~10 nm) electron-dense region on the inner
 380 membrane (Figure 5b, right); this may represent scenario II of the confocal images (Figure 5a).
 381 These two scenarios correlate with two types of LacZ^{mRuby-Pop} condensates, dome-shaped
 382 (more frequent) and spherical (less frequent) that are observed by confocal laser-scanning
 383 microscopy at the cell poles of BW25113 LacY^{mEos-Pop}-LacZ^{mRuby-Pop} cells (Figure 5a). The two
 384 scenarios can be rationalized when LacY and LacZ have different expression levels: Scenario I
 385 would occur when the levels are similar, and Scenario II if LacZ is expressed at a higher level
 386 than LacY. We conclude that LacY^{Pop} and LacZ^{Pop} form heterocondensates of varying
 387 architectures that are anchored to the inner membrane of *E. coli*.

388

389

390



391

392 **Figure 5. LacY^{Pop} and LacZ^{Pop} heterocondensates *in vivo*.** (a) Confocal laser-scanning
 393 microscopy of *E. coli* BW25113 LacY^{mEos}-LacZ^{mRuby}, BW25113 LacY^{mEos-Pop}-LacZ^{mRuby},
 394 BW25113 LacY^{mEos}-LacZ^{mRuby-Pop} and BW25113 LacY^{mEos-Pop}-LacZ^{mRuby-Pop}, co-expressing PopTag and non-
 395 PopTag versions of membrane LacY^{mEos} and cytoplasmic LacZ^{mRuby} proteins. (I) and (II) are
 396 pointing to cells with different scenarios of LacY^{mEos-Pop}-LacZ^{mRuby-Pop} interaction (described in
 397 the main text). (b) Transmission electron microscopy images of 100 nm thin sections of

398 BW25113 LacY^{mEos-Pop}-LacZ^{mRuby-Pop} cells showing scenarios I and II. A dashed orange line
 399 outlines the apparent electron-dense regions. Panel **a** highlights cells with scenarios I and II,
 400 which are enlarged in the insets of panel **b**. **(c)** *In vivo* β -galactosidase activity in *E. coli*
 401 BW25113 Δ lacY LacY LacZ, BW25113 Δ lacY LacY^{Pop}-LacZ, BW25113 Δ lacY LacY-LacZ^{Pop} and
 402 BW25113 Δ lacY LacY^{Pop}-LacZ^{Pop}. The β -MUG conversion rate (Figure S9) was corrected for the
 403 amount of protein, determined by fluorescent imaging of SDS-PAGE gels (Figure S10) and
 404 normalized to the activity in BW25113 Δ lacY LacY LacZ strain; referred to in the figure as
 405 adjusted LacZ activity. Data are presented as mean \pm SD, n = 4.

406

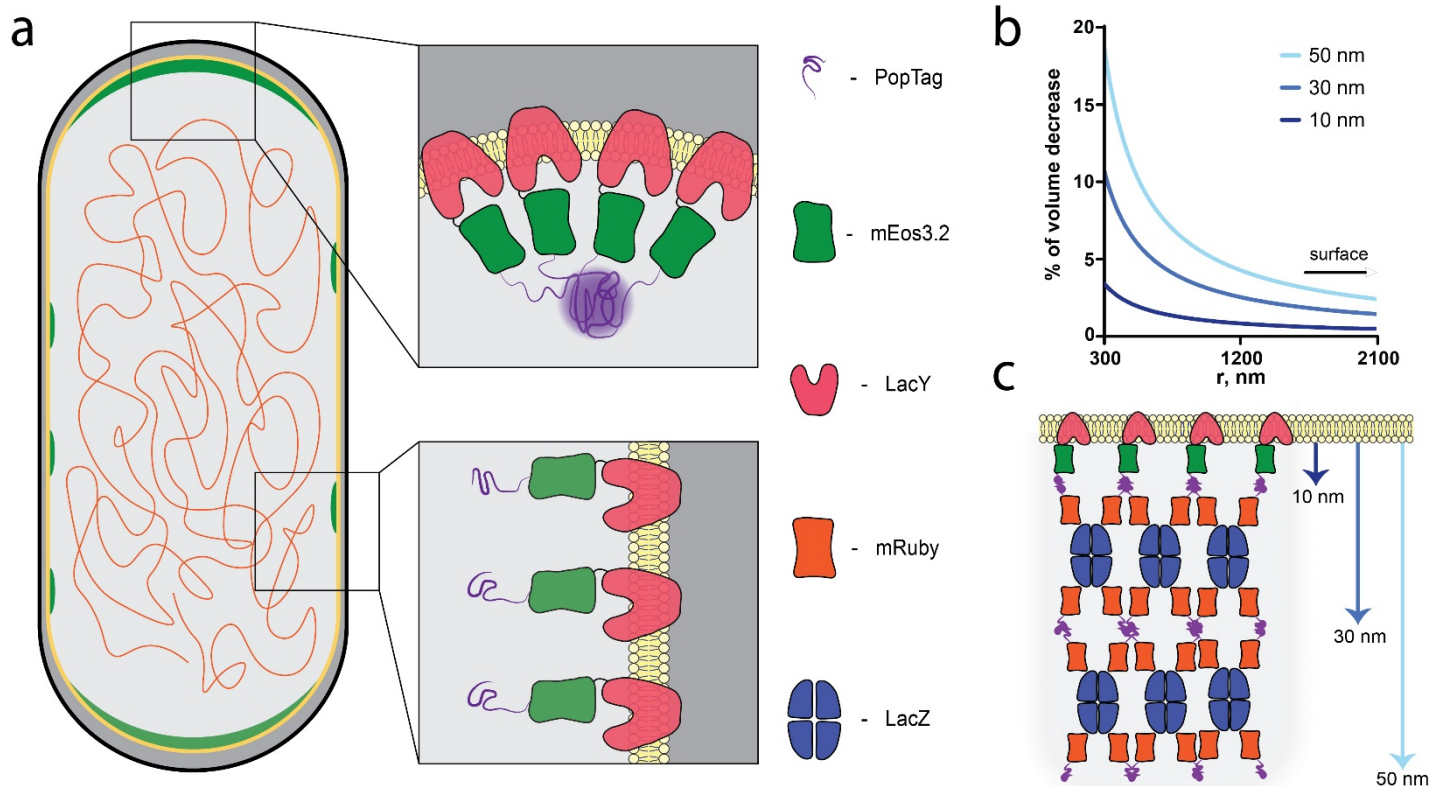
407 We then assessed the activity of LacY and LacZ in the heterocondensates. We
 408 constructed *E. coli* strains without mEos3.2 and mRuby to enable fluorescent read-out of LacZ
 409 activity with 4-methylumbelliferyl β -D-galactopyranoside as substrate^{29,30}. The new strains are
 410 named BW25113 Δ lacY LacY-LacZ, BW25113 Δ lacY LacY^{Pop}-LacZ, BW25113 Δ lacY LacY-LacZ^{Pop}
 411 and BW25113 Δ lacY LacY^{Pop}-LacZ^{Pop} (for details see Table 1). LacY activity was similar across
 412 all strains as evaluated by ¹⁴C-lactose uptake measurements (Figure S8). The fluorescent
 413 substrate, 4-methylumbelliferyl β -D-galactopyranoside (β -MUG), is transported by LacY³⁰ and
 414 hydrolyzed by LacZ. The transport negative strain, BW25113 Δ lacY, shows a slight decrease in
 415 signal over time, which does not reflect β -galactosidase activity. Strains expressing LacY and
 416 LacZ, with or without PopTag, hydrolyze β -MUG, and we estimated the β -galactosidase activity
 417 from the slope of the linear increase of fluorescent signal over time (Figure S9). The
 418 fluorescence data were adjusted for the amounts of expressed β -galactosidase, determined
 419 by fluorescence imaging of SDS-PAGE separated *E. coli* lysates of LacZ-mRuby fusions, to
 420 obtain the specific β -galactosidase activity (Figure S10). The activities of LacZ in all strains were
 421 normalized to the mean activity in BW25113 Δ lacY LacY-LacZ cells, which was 1.00 \pm 0.03 a.u.
 422 The activity increases to 1.62 \pm 0.05 a.u. in BW25113 Δ lacY LacY-LacZ^{Pop} cells, but decreases to
 423 0.80 \pm 0.02 a.u. and 0.82 \pm 0.04 a.u. in BW25113 Δ lacY LacY^{Pop}-LacZ and BW25113 Δ lacY LacY^{Pop}-
 424 LacZ^{Pop} cells, respectively (Figure 5c). Clearly, the activity of β -galactosidase is highest when
 425 the protein is present in homocondensate and somewhat reduced in heterocondensates with
 426 LacY.
 427

428 Discussion

429 Coacervate-membrane interactions and membrane-anchored biomolecular
 430 condensates have been observed³¹, but mechanistic insight into their cellular organization and
 431 function is lacking, and membrane-anchored cellular heterocondensates have not been
 432 studied at all. We now provide a systematic study in this direction, using lactose metabolism
 433 in *Escherichia coli* as test case and a small (7 KDa) condensation tag, derived from the PopZ
 434 protein from *Caulobacter vibrioides*, to induce condensation. Figure 2c shows that the PopTag
 435 has three amphipathic α -helices with a high hydrophobic moment, and the hydrophobic faces
 436 of these putative helices form the “stickers” for condensation as shown by our MD

437 simulations. The PopTag provides an orthogonal, non-native tool to study liquid-liquid phase
 438 separation both *in vitro* and *in vivo*.

439 Using fluorescence microscopy, we show that LacY^{mEos-Pop} forms larger biomolecular
 440 condensates at the cell poles and smaller ones in the lateral membrane of *E. coli* (Figure 1).
 441 Molecular dynamics simulations confirm that the condensate formation is driven by
 442 hydrophobic interactions between PopTag's amphipathic α -helices. Using electron
 443 microscopy, we confirm that LacY^{mEos-Pop} condensates localize on the cytoplasmic face of the
 444 inner membrane without disturbing membrane shape and integrity (Figure 1g). From the ¹⁴C-
 445 lactose uptake assays, we see that LacY^{mEos-Pop} is functional within condensates (Figure 4a). In
 446 FRAP experiments with LacY^{mEos-Pop}, we observe only partial (~20%) fluorescence recovery at
 447 the bleached cell pole without major decrease in fluorescence at the opposite pole, indicating
 448 that on the observed time scales the protein mostly redistributes between the pole and the
 449 lateral membrane, but not between two poles (Figure 1d, Figure S1). We argue that the
 450 number of multivalent interactions between the PopTags is on average lower in the small
 451 lateral membrane condensates than in the pole condensates, enabling LacY^{mEos-Pop} to escape
 452 more easily than from the larger pole condensates (smaller perimeter/surface area ratio). A
 453 partial fluorescence recovery has also been observed for cytoplasmic mCherry-PopTag
 454 fusion¹⁶. Unlike cytoplasmic mCherry-PopTag, LacY^{mEos-Pop} forms multiple small condensates
 455 in the lateral membrane alongside with two major polar condensates. A localization pattern
 456 akin that of LacY^{mEos-Pop} has been observed for the natively phase-separated membrane
 457 protein Rv1747 in *M. tuberculosis*⁸, but the functional implications of the heterogenous
 458 membrane localization have not been studied.



459

460 **Figure 6. Model of curvature-driven localization of membrane-anchored biomolecular**
 461 **condensates. (a)** Localization pattern of LacY-mEos3.2-PopTag condensates (green) in rod-
 462 shaped *E. coli*. Light grey color represents cytoplasm, dark grey – periplasm, yellow line is inner
 463 membrane, and orange is nucleoid. LacY-mEos3.2-PopTag in the lateral membrane does not
 464 create large phase-separated condensates as the local PopTag concentration is limited by the
 465 surface-to-volume ratio. Only some small and dynamic condensates are formed. The smaller
 466 cytoplasmic volume for the same surface area (higher surface-to-volume ratio) at the cell pole
 467 results in a higher concentration of PopTags, which favors condensate formation. **(b)** Pre-
 468 membrane volume at 10, 30 and 50 nm thickness as a function of membrane radius (300 nm
 469 → infinity). The decrease in pre-membrane volume is 3.4, 10.7 and 18.7 % for a thickness of
 470 10, 30 and 50 nm, respectively. **(c)** Schematic representation of membrane-anchored
 471 biomolecular condensate and heterocondensate. Approximate distance from the membrane
 472 is based on EM data and structures of LacY, LacZ and fluorescent proteins. One layer of
 473 LacZ^{mRuby-Pop} condensate on top of LacY^{mEos-Pop} has a maximal predicted thickness of ~30 nm
 474 and two layers of LacZ^{mRuby-Pop} yield ~50 nm.

475

476 Our experiments with cell shape and nucleoid content perturbations shed light on the
 477 mechanism governing the predominant pole localization of LacY^{mEos-Pop} condensates. Using
 478 cells harboring multiple nucleoids and cells with degraded nucleoid, we show that nucleoid
 479 exclusion is not the driving force for formation of LacY^{mEos-Pop} condensates at the poles (Figure
 480 2abc). Instead, the membrane geometry and most likely curvature is important for pole
 481 localization of the membrane condensates: the LacY^{mEos-Pop} condensates redistribute in the
 482 membrane upon spheroplast formation, and localize to the high-curvature regions in
 483 osmotically upshifted spheroplasts (Figure 3de, Movie S2).

484 We hypothesize that local changes in the surface-to-volume ratio of the pre-
 485 membrane condensate plays a role in the curvature-driven polar localization of LacY^{mEos-Pop}.
 486 We consider a model, where PopTag drives the condensation of LacY^{mEos-Pop} within a pre-
 487 membrane volume of thickness d , which is determined by the length of PopTag and the linker
 488 (connected to the last transmembrane segment of LacY). For the same area of membrane
 489 surface covered by LacY, a smaller pre-membrane volume is accessible for PopTag if the
 490 membrane is curved, leading to a higher local concentration that is critical for condensation
 491 (Figure 6b). An increase in concentration enhances phase-separation of LacY^{mEos-Pop} at the
 492 areas of the higher curvature. For the 10-nm thick pre-membrane volume, the expected local
 493 increase of the concentration at the cell pole with radius of about 300 nm is only 3%. Although
 494 this change in concentration is most likely insufficient to be a sole reason for the observed
 495 polar localization of LacY^{mEos-Pop}, we speculate that it can act synergistically with other
 496 mechanisms governing the distribution of membrane protein-based condensates. Alternative
 497 mechanisms that could affect polar localization of LacY^{mEos-Pop} condensates include: (1) specific
 498 interactions with biomolecules (e.g. cardiolipin^{32,33}) partitioning at the cell poles, (2) physical
 499 trapping of condensates by large membrane protein assemblies at the cell poles (similar to
 500 trapping of chemoreceptors by Tol-Pal complexes³⁴), and (3) progressive displacement of the
 501 cell wall components toward the poles upon cell elongation (similar to displacement of ActA

502 in *Listeria monocytogenes*^{35,36}). However, these mechanisms may be disrupted when cells are
 503 spheroplasted and subsequently plasmolysed. Yet, LacY^{mEos-Pop} localizes to the highly curved
 504 concave regions of the cytoplasmic membrane upon osmotic upshift.

505 Cells with LacY^{mEos-Pop} accumulate lactose to higher final concentrations (Figure 4b),
 506 suggesting either higher import activity of LacY^{mEos-Pop} compared to LacY^{mEos} or a bigger cell
 507 volume, assuming that the driving force for lactose-proton symport remains the same. The
 508 transport of lactose and proton proceeds via the formation of a ternary complex with the LacY
 509 protein, but the coupling (ternary lactose-H⁺-LacY complex) is not always strict, which can lead
 510 to different accumulation levels at the same driving force^{37,38}. The coupling efficiency of
 511 secondary active transporters like LacY can be altered by mutations or a different membrane
 512 environment. It is thus possible that the higher accumulation by LacY^{mEos-Pop} reflects a higher
 513 coupling efficiency due to altered by protein-protein interactions within the condensate or
 514 and by the distinct protein and lipid environment of the cell pole. Also, the PopTag scaffold
 515 could mechanically support the membrane, explaining the lesser deformations in LacY^{mEos-Pop}
 516 cells upon osmotic upshift (Figure 4e). The PopTag scaffold may also affect other biophysical
 517 properties of the membrane, *e.g.* viscosity, as was previously shown *in vitro* for other
 518 membrane-associated biomolecular condensates^{39,31}. However, the important conclusion
 519 that we draw is that the condensation of LacY does not negatively affect its activity and may
 520 even increase the performance of the protein.

521 Using PopTag, we created a heterocondensate of a cytoplasmic enzyme and a
 522 membrane transport protein, LacZ and LacY, *in vivo*. The β -galactosidase activity of LacZ^{Pop} is
 523 ~1.6 times higher than that of LacZ, which is in line with the increase of LacZ activity in peptide-
 524 peptide condensates *in vitro*, also using β -MUG as substrate²⁹. The increased activity of LacZ
 525 in condensates, both *in vivo* and *in vitro*, could be due to the stabilization of tetrameric LacZ.
 526 The condensate microenvironment with higher local LacZ concentration might shift the
 527 oligomeric equilibrium towards active tetramers⁴⁰. When LacY and LacZ form a
 528 heterocondensate, the activities of both proteins are slightly decreased, for which we have no
 529 direct explanation. If LacZ^{mRuby-Pop} protein is added to the model of curvature-dependent polar
 530 localization of LacY^{mEos-Pop} (Figure 6bc), the thickness of the pre-membrane volume increases
 531 to ~50 nm, resulting in a more pronounced, up to 20%, local increase of the concentration.
 532 This makes the formation of heterocondensates at the poles more favorable than the
 533 assembly of homotypic LacY^{mEos-Pop} condensates.

534
 535 In conclusion, we show that LacY^{Pop} forms biomolecular condensates that localize at the cell
 536 poles of *E. coli* in a curvature-dependent manner; under some conditions condensated LacY^{Pop}
 537 outperforms the wild-type LacY in transport activity and can form functional
 538 heterocondensates with its metabolic partner LacZ^{Pop}. Having characterized the structure and
 539 interactions of LacZ^{Pop} membrane condensates experimentally and computationally,
 540 engineering specialized condensation tags with alternative interaction modes may further
 541 optimize the coupling between membrane transporters and metabolic networks. We propose
 542 that the variety of natively-disordered regions in a wide range of integral membrane proteins

543 warrant further investigation^{8,41-43}. They may not solely be regulatory sites that tune protein
544 activity via post-translational modifications but also play a role in the supramolecular
545 organization of membrane-bound complexes. Our research provides a framework to engineer
546 cells and exploit the co-localization of molecules in metabolic networks, stabilize proteins in
547 biomolecular condensates, and/or tune enzymatic efficiency and protein localization *in vivo*.
548 Collectively, our findings contribute to the emerging field of liquid-liquid phase separation and
549 the engineering of spatially-controlled metabolic reactions networks and their coupling to
550 membrane-bound processes.

551

552 Materials and methods

553 Strains and plasmids

554 *E. coli* strain BW25113 [F-, Δ (araD-araB)567, Δ lacZ4787(:rrnB-3), λ -, *rph*-1, Δ (*rhaD*-
555 *rhaB*)568, *hsdR514*] was used for most experiments. For storage and cloning we used *E. coli*
556 DH5 α [[F-, Δ (*argF-lac*)169, φ 80d*lacZ58*(M15), Δ *phoA8*, *glnX44*(AS), λ -, *deoR481*, *rfbC1*,
557 *gyrA96*(*NaR*), *recA1*, *endA1*, *thiE1*, *hsdR17*]. All strains and plasmids used are found in Table
558 1. Plasmids were constructed with the USER cloning protocol and transformed to *E. coli* via
559 the heat-shock method and subsequently checked via Sanger sequencing by Eurofins
560 Genomics. Plasmid DNA was isolated with the NucleoSpin Plasmid kit (MACHEREYNAGEL). All
561 protein sequences and primers used in this study are shown in Supplementary Tables 1 and 2
562 respectively.

563 Culturing conditions

564 Antibiotic concentrations used as a selective marker were 100 μ g/ml ampicillin
565 (dissolved as 1000x stock) in 50% EtOH, 20 μ g/ml chloramphenicol (dissolved as 1000x stock)
566 and 10 μ g/ml tetracycline (dissolved as 1000x stock). Lysogeny broth (LB) was prepared using
567 standard recipe and sterilized by autoclaving. Mops-buffered minimal media (MBM) was
568 prepared as described in^{19,44}. All measurements were performed in the MBM media after
569 overnight preculturing in LB followed by overnight preculturing in MBM media as described in
570^{19,20}. Briefly 3 mL of LB media supplemented with antibiotic(s), if strains harbor plasmids, was
571 inoculated with a single colony of *E. coli* and grown overnight at 30°C with shaking at 180 rpm,
572 after which the preculture in LB was diluted 100-fold in MBM supplemented with 0.1% (v/v)
573 glycerol plus antibiotic(s) and incubated overnight at 30°C with shaking at 180 rpm. On the
574 next day, the MBM preculture was diluted into fresh, prewarmed MBM with 0.1% (v/v)
575 glycerol plus antibiotic(s) to a final OD₆₀₀ of 0.05 and grown for the needed amount of time,
576 typically 4 h until an OD₆₀₀ of 0.15 was reached. Unless stated otherwise, expression of *lacY*
577 fusion genes from pBAD was induced by 0.1% L-arabinose for 4 hours, expression of *lacZ* fusion
578 genes from pACYC was induced by 0.000001% L-rhamnose for 4 hours.

579 For all microscopy measurements cells were grown in 3 mL of MBM media for 4 hours.
580 1 mL of cell culture was spun down and resuspended in 100 μ L of remaining media. 2 μ L of
581 cell culture were put on cleaned (by sonication in 5M KOH) 1.5H high-precision glass slides

582 (170 μ m thickness, Carl Roth GmbH & Co KG) and immobilized by agarose pads as described
 583 elsewhere^{19,20}.

584 For electron microscopy, lactose transport and β -galactosidase activity assays, cells
 585 were grown using the following protocol: 3 mL of LB preculture (with the appropriate
 586 antibiotic(s)) was inoculated with a single colony of the appropriate *E. coli* strain and grown
 587 overnight at 30 °C with shaking at 180 rpm. The next day, the LB preculture was diluted 100x
 588 into 20 mL of MBM minimal media supplemented with 0.1% glycerol plus antibiotic(s) and
 589 grown overnight at 30 °C with shaking at 180 rpm. The next day, the MBM preculture was
 590 diluted into 100 mL of MBM media with 0.1% glycerol plus antibiotic(s) to reach a final OD₆₀₀
 591 of 0.05. Induction of genes coding for LacY and LacZ variants was done by adding 500 μ L of
 592 20% arabinose (f.c. 0.1%) and 100 μ L of 0.001% rhamnose (f.c. 0.000001%), respectively, and
 593 the cells were incubated for 4 hours to reach an OD₆₀₀ of ~0.15.

594 To block the division of *E. coli* 20 μ g/ml of cephalexin dissolved in MQ water was added
 595 to the cells at the moment of dilution to OD₆₀₀ of 0.05 and treatment was continued for 4 or
 596 7 hours.

597 For nucleoid degradation *E. coli* LY177 [Δ recA-Tc *ydeO*::*I-Sce1*^{CS}, *ilvA*::*I-Sce1*^{CS}] was
 598 used²³. Expression of the *I-Sce1* gene was induced with 0.2% L-Arabinose for 2 hours from pSN1
 599 and *lacY* fusions were expressed from pACYC vector and 0.5% L-Rhamnose as inducer. In the
 600 liquid media and agarose plates for *E. coli* LY177, carrying pACYC, 0.2% glucose was used to
 601 reduce the leaky expression of the gene coding for *I-Sce1* endonuclease (J. Losa, personal
 602 communication, 2024). To obtain the *E. coli* LY177 with two plasmids, the cells were first
 603 transformed with the pACYC vector, carrying genes of the *lacY* variants, and plated on agar
 604 with chloramphenicol plus tetracycline. Next, a new batch of competent cells was made from
 605 these cells, grown in the presence of chloramphenicol plus tetracycline. They were
 606 subsequently transformed with pSN1, carrying endonuclease the *I-Sce1* gene, and plated on
 607 agar with chloramphenicol, tetracycline, ampicillin supplemented with 0.2% glucose. The cells
 608 were used within a week to prevent nucleoid degradation due to leaky expression of *I-Sce1*.

609 The protocol for spheroplasts preparation was adapted from^{24,25}. Cells were grown in
 610 the presence of 20 μ g/ml cephalexin for 4 hours, while the gene of interest was expressed.
 611 Then 1 ml of cell culture was concentrated two times by centrifugation at 10,000 rpm in a
 612 Spectrafuge™ 16M centrifuge for 1 min. To 500 μ L of cell culture 500 μ L of 2M glucose
 613 solution, 5 μ L of 200 μ g/mL lysozyme plus 5 μ L of 0.5 M EDTA (pH 8.0) were added, and the
 614 cells were incubated at room temperature for 15 min. 2.5 μ L of 1 M MgCl₂ was added to
 615 quench the spheroplasting and cells were concentrated to 100 μ L.

616

617 **Wide-field fluorescence microscopy**

618 A Zeiss Axio Observer microscope with 100x oil immersion objective (1.4 NA) was used
 619 for imaging of *E. coli* cells. Fluorescence of mEos3.2 green state was excited by 470 nm LED
 620 and the emission was collected in the 500-550 nm wavelength range. For nucleoid staining we
 621 used DAPI at a final concentration of 15 μ M (incubated for 15 min), and the fluorescence was

622 excited by 365 nm LED and the emitted light was collected in the 420-470 nm range. Phase
 623 contrast for intact bacterial cell or brightfield images for spheroplasts were also collected.

624 **Fluorescence recovery after photobleaching (FRAP)**

625 FRAP measurements were performed on Zeiss LSM 710 ConfoCor 3 (Plan-Apochromat
 626 100x/1.40 Oil objective) microscope for LacY-mEos3.2 and on Leica Stellaris 8 (Plan-
 627 Apochromat 63/1.40 Oil objective) microscope for LacY-mEos3.2-PopTag.

628 Bleaching and fluorescence recovery were recorded for multiple cells in a field of view.
 629 The 488 nm laser was used for both bleaching and detection of LacY variants. Because the
 630 intensity of the readout laser also bleaches LacY^{mEos} and the mobility of the protein is relatively
 631 high, we also recorded the fluorescent signal from the non-bleached cell pole and used this to
 632 correct the recovery for bleaching during readout.

633 **Single-molecule displacement mapping (SMdM)**

634 SMdM measurements were performed as described previously^{19,20} with some
 635 modifications. Briefly, a 405 nm laser pulse (OBIS 405 LX, 50 mW max. power) was used to
 636 photoconvert mEos3.2 from a green fluorescent state (507 nm ex. / 516 nm em.) to red (572
 637 nm ex. / 580 nm em.), and two readout beams of 561 nm laser (OBIS LS 561-150) were used
 638 with time separation (Δt) of 10 ms. Time separation between the excitation 561 nm pulses
 639 was increased from 1.5 ms to 10 ms as mobility of slow diffusing proteins is better captured
 640 at higher Δt values⁴⁵. The emitted signal was collected by a EM-CCD camera (C9100-13,
 641 Hamamatsu), using a ET 605/70 M bypass filter (Chroma).

642 ThunderSTORM plugin of ImageJ (<https://zitmen.github.io/thunderstorm/>) was used
 643 for the peak detection to obtain single-protein localizations along with the localization
 644 uncertainty values. We used localization uncertainty values for the correction of the
 645 measured diffusion coefficient. Knowing the localization uncertainty, we can estimate the
 646 apparent diffusion coefficient, which is related to this uncertainty ($D_{loc.unc}$), using the
 647 following equation:

$$648 \quad \sqrt{\sigma_{start}^2 + \sigma_{end}^2} = \sqrt{2nD_{loc.unc}\Delta t} \quad (1)$$

649 Where n is number of dimensions, σ_{start} and σ_{end} are uncertainties in localization of
 650 starting and ending positions of the protein displacements over the Δt time period. Assuming
 651 that the localization uncertainties for the start and end positions are equal and that $n = 2$,
 652 equation 1 simplifies to:

$$653 \quad D_{loc.unc} = \frac{\sigma_{mean}^2}{2\Delta t} \quad (2)$$

654 To obtain the diffusion coefficient of moving proteins, the probability density
 655 distribution of measured displacements as a function of time separation (Δt) was fitted with
 656 an adjusted probability density function (PDF) of a 2-dimensional random-walk diffusion
 657 model with background correction and normalized for the maximum search radius⁴⁶.

658

$$p(r, \Delta t) = \frac{1}{1 - e^{-\frac{r_{max}^2}{4D_L \Delta t}} + \frac{b}{2} r_{max}^2} \left(\frac{2r}{4D_L \Delta t} e^{-\frac{r^2}{4D_L \Delta t}} + br \right) \quad (3)$$

659 Where D_L is the lateral diffusion coefficient, r is the peak-to-peak displacement, Δt is
 660 the time separation between 561 nm readout laser pulses (10 ms in this case), b is a
 661 background correction coefficient, and r_{max} is 200 nm. Because proteins with lower mobility
 662 are more affected by localization uncertainty, we subtract the $D_{loc.unc}$ from the D_L to correct
 663 for this effect.

664 To reconstruct diffusion maps we binned each cell into square selections with a side of
 665 100 nm and fitted the displacements starting within a bin with equation 3. This was done for
 666 bins with at least 100 displacements.

667 **Photoactivated localization microscopy (PALM)**

668 For super-resolution microscopy, the same home-built setup was used as for SMdM
 669 measurements. To convert and excite mEos3.2 fluorescent protein we utilized the same pulse
 670 pattern as for SMdM measurements. Peak detection was done using ThunderSTORM plugin
 671 (<https://zitmen.github.io/thunderstorm/>) for ImageJ software, using appropriate camera
 672 parameters. Super resolution images were reconstructed using a custom Python script⁴⁷.

673 **Confocal microscopy**

674 The Leica Stellaris 8 microscope with white light laser was used to localize different
 675 variants of LacY-mEos3.2 and LacZ-mRuby in *E. coli* cells. For excitation of mEos3.2, 489 nm
 676 laser light was used and the emitted light in the 500-581 nm range was collected; 560 nm laser
 677 was used to excite mRuby and emitted light in the range 581-700 nm was collected.

678 **Electron microscopy**

679 Cells were grown as described in “Culturing conditions” section. *E. coli* cells were
 680 concentrated by centrifugation at 4,000 x g to the minimal volume possible (paste-like
 681 suspension) and transferred to a 3 mm copper gold-plated type B (flat-surfaced) carrier
 682 (Leica). Cells immobilized by high pressure freezing (EM ICE, Leica) were freeze-substituted in
 683 1% (w/v) OsO₄ plus 0.5% uranyl acetate in acetone with 5% water, using the quick freeze
 684 substitution method⁴⁸. Samples were embedded in Epon resin and ultra-thin sections of
 685 approximately 100 nm were collected on formvar-coated and carbon evaporated copper grids
 686 and inspected using a TALOS L120C (Thermo Scientific) transmission electron microscope
 687 (TEM). For the ultrastructural analysis, we have selected cells where the inner and outer
 688 membranes are clearly visible and a periplasm thickened at the cell pole; we excluded cells
 689 that were sectioned at high angles relative to the long axis of the cell.

690

691 **Molecular dynamics simulations**

692 Protein structures (LacY, LacY^{Pop}, and PopTag) were modelled using AlphaFold3⁴⁹. All
 693 simulations were performed using Gromacs 2024.3 with the Martini 3 force field⁵⁰⁻⁵².

694 Topologies and initial conformations for all protein structures were generated from
695 their all-atom counterparts using Martinize2⁵³. The Martini3 protein model requires explicit
696 assignment of secondary structure elements during model building. For the PopTag, we
697 assigned these structural elements based on the Jpred tool and all-atom simulations from a
698 previous study, since AlphaFold predictions struggle to represent the ensemble characteristics
699 of intrinsically disordered regions^{54–56}. The three helices motifs of the PopTag were modelled
700 as H1 (residues 14 – 31), H2 (residues 40 – 58), and H3 (residues 62 – 76), with remaining
701 residues modelled as coils. For the intrinsically disordered region at the N-terminus of PopTag
702 (residues 1 – 13), Martini parameters were tuned using the -idr-tune flag in Martinize2⁵⁷.

703 Placing the proteins into the simulation box was done using Bentopy, while the
704 membranes were constructed using the *insane* tool^{58,59}. Lipid compositions were chosen to
705 represent the *E. coli* inner membrane (75% POPE, 20% POPG, 5% cardiolipin)⁶⁰. During
706 system preparation, each simulation box was solvated, neutralized, and NaCl was added to
707 reach a concentration of 150 mM. The slab condensate model was constructed with 100
708 molecules contained within the central 15 nm of a 15 × 15 × 50 nm simulation box
709 resulting in a concentration of 15mM of protein. For the membrane simulations, 9 copies of
710 LacY or LacY^{Pop} were placed in a regular grid configuration into a membrane of 35nm x 35nm
711 maintaining equal distances between adjacent membrane proteins.

712 The initial configurations underwent energy minimization using Gromacs' steepest
713 descent algorithm, followed by equilibration and production simulations. Equilibration was
714 conducted for 50 ns using a 10 fs timestep, while production runs used a 20 fs timestep for
715 simulation time of 20 μs. Temperature and pressure were regulated during equilibration and
716 production simulations using the v-rescale thermostat and c-rescale barostat respectively. All
717 simulations employed semi-isotropic pressure coupling. For membrane simulations, pressure
718 was maintained at 1 bar ($\tau_p = 12 \text{ ps}$, $\beta = 3e^{-4} \text{ bar}^{-1}$). For slab condensate simulations, the
719 pressure along the longest box axis was set to be incompressible, while default parameters
720 were applied along other axes. All simulations were conducted at 300 K ($\tau_t = 1 \text{ ps}$) with
721 separate coupling groups for solvent, lipid, and protein when applicable.

722 Other nonbonded simulation parameters followed Martini3 recommendations for
723 Gromacs, with specific settings for large membranes (verlet – buffer – tolerance =
724 –1, rlist = 1.35 nm)^{52,61,62}. All simulations were performed in triplicate for better statistics
725 on the results. Analysis of the simulation data was performed using the MDAnalysis Python
726 library^{63,64}. The protein-protein contacts were identified using a distance-based criterion, with
727 residues considered in contact when their backbone beads are within 10 Å of each other. The
728 number of protein clusters was defined as the number of distinct protein groups where
729 proteins within each group shared at least one residue-residue contact with another protein
730 in that group. Within these clusters, the number of protein-protein contacts was quantified as
731 the count of unique protein pairs in contact. For clarity, the time evolution traces of the
732 protein cluster metrics were smoothed with a median filter with a window size of 25 ns. To
733 create the contact maps, we calculated the specific residue-residue contacts across all
734 simulation frames and determined their frequency. Snapshots of the molecular dynamics

735 trajectories were rendered using Visual Molecular Dynamics (VMD) software⁶⁵ and figures
736 were made using Matplotlib⁶⁶.

737

738 **Transport assays**

739 Cells were grown as described in “Culturing conditions” section. Part of the cells were
740 taken for imaging and the rest was used for transport assays. After harvesting by
741 centrifugation (10 min at 4,000 x g), the cells were resuspended to an OD₆₀₀ of ~25 in MBM
742 media plus 10 mM glucose, which was also used as assay buffer. [D-glucose-1-¹⁴C] lactose (56
743 mCi/mmol) was purchased from American Radiolabeled Chemicals. For the assay
744 concentrated cells were diluted into MBM media plus 10 mM glucose to an OD₆₀₀ of 1 and
745 prewarmed at 30°C. At time zero of the assay ¹⁴C-lactose was added to a final concentration
746 of 10 µM. The assay volume was 150 µL and at given time intervals (10, 40, 70, 100 and 150
747 sec), samples of 25 µL were taken and the transport reaction was quenched with 2 mL ice-cold
748 0.1 M LiCl, and the mixture was filtered immediately over prewetted nitrocellulose filters with
749 a pore diameter of 0.45 µm (Protean, Cytiva). Subsequently, the filters were washed with 2
750 mL ice-cold 0.1 M LiCl and then dissolved in 2 mL Ultimagold TM scintillation fluid (Perkin
751 Elmer). Radioactivity, reflecting the uptake of ¹⁴C-lactose, was determined with a Perkin Elmer
752 Tri-carb 2800TR scintillation counter.

753 For uptake of lactose under osmotic stress conditions, 12 µL of the MBM media in the
754 assay and the quench buffer was replaced by 2 or 4 M NaCl to reach final additional
755 concentration of 160 mM and 320 mM respectively.

756 **β-Galactosidase activity assay**

757 Cells were grown as described in “Culturing conditions” section. Cells are harvested by
758 centrifugation at 4,000 x g at 4 °C for 10 min and concentrated to a final OD₆₀₀ of 5 in
759 phosphate-buffered saline (PBS, 0.40 g NaCl, 0.01 g KCl, 0.07 g Na₂HPO₄, 0.01 g KH₂PO₄ in 50
760 mL MQ water, pH 7.4) on ice. 190 µL of cells were added to a black µClear Flat Bottom 96-well
761 plate for fluorescence measurements (Greiner). 10 µL of 1mM 4-methylumbelliferyl β-D-
762 galactopyranoside (β-MUG) was added to each well, to reach a final concentration of 50 µM.
763 Upon cleavage by β-galactosidase the emission maximum of β-MUG shifts from 375 to 445
764 nm; the increase at 445 nm was used to determine the β-galactosidase activity. The Spark
765 Multimode plate reader (TECAN) was used to monitor the progress of the reaction at 445 nm
766 at 30 °C with β-MUG excitation at 320 nm wavelength. Emission spectra were measured in the
767 range of 345 – 550 nm, immediately after β-MUG addition and after the time-series
768 measurement (Figure S11). Fluorescence at 445 nm wavelength was measured every minute
769 for 19 minutes.

770 **Statistical analysis**

771 Data in the text presented as mean ± SD unless otherwise specified. Normality of data
772 distribution was tested by the Shapiro-Wilk test. Two-side Student *t*-test was used at the
773 significance level of 5 percent to compare mean values of two datasets. Linear or exponential
774 plateau functions were fitted to the datasets using relevant regression models, and

775 parameters of these models such as slope or plateau level were used to determine parameters
776 for e.g. ¹⁴C-lactose uptake. GraphPad Prism 10 software was used to perform all statistical
777 tests and to make plots.

778 Code availability

779 The developed code for modulating laser pulses, using a PCI-6602 programmable card
780 (National Instruments), for SMdM analysis and PALM reconstruction is available on the Github
781 repository of Membrane Enzymology Laboratory:
782 <https://github.com/MembraneEnzymology/>

783 Data availability

784 The source data behind the graphs in the paper can be found in Supplementary Data.
785 The raw data is available from the corresponding author upon request.

786 Authors contributions

787 **D.L.** and **S.S.** cloned and expressed the genes. **D.L.**, **S.S.** and **I.M.** performed wide-field
788 fluorescence microscopy and FRAP measurements. **D.L.** performed SMdM and confocal
789 measurements. **D.L.** performed experiments with nucleoid degradation, division inhibition
790 and spheroplasts formation. **J.A.S.** performed the MD simulations. **G.K.S-W** performed ¹⁴C-
791 lactose uptake experiments and SDS-PAGE. **R.de.B.** performed high-pressure freezing and
792 transmission electron microscopy. **C.M.P.** provided IT supervision and helped **D.L.** with
793 analysis methods development. **D.L.** and **B.P.** conceptualized the project. **D.L.**, **I.M.**, **J.A.S.**,
794 **S.J.M** and **B.P.** analyzed and discussed the data. Manuscript was written by **D.L.**, **I.M.** and **B.P.**
795 with contribution from all authors.

796 Declaration of interests

797 The authors declare that they do not have competing interests.

798 Acknowledgements

799 We would like to thank Lyan van der Sleen for data discussions and José Vila Chã Losa and
800 Matthias Heinemann for *E. coli* LY177 and BW25113 *ΔlacY*. The work of Dmitrii Linnik, Jan A.
801 Stevens, Siewert-Jan Marrink and Bert Poolman was funded by the NWO National Science
802 Program "The limits to growth" (grant number NWA.1292.19.170). Additionally, the work of
803 Bert Poolman was supported by the NWO Gravitation program "Building a synthetic cell"
804 (BaSyC). Ivan Maslov thanks the European Union for funding his research under the HORIZON
805 TMA MSCA Postdoctoral Fellowships action (project MemProDx, 101149735).

806 References

807

808 1. Azaldegui, C. A., Vecchiarelli, A. G. & Biteen, J. S. The emergence of phase separation as
809 an organizing principle in bacteria. *Biophysical Journal* **120**, 1123–1138 (2021).

810 2. Alberti, S. & Hyman, A. A. Biomolecular condensates at the nexus of cellular stress,
811 protein aggregation disease and ageing. *Nat Rev Mol Cell Biol* **22**, 196–213 (2021).

812 3. Spannl, S., Tereshchenko, M., Mastromarco, G. J., Ihn, S. J. & Lee, H. O. Biomolecular
813 condensates in neurodegeneration and cancer. *Traffic* **20**, 890–911 (2019).

814 4. Saini, B. & Mukherjee, T. K. Biomolecular Condensates Regulate Enzymatic Activity under
815 a Crowded Milieu: Synchronization of Liquid–Liquid Phase Separation and Enzymatic
816 Transformation. *J. Phys. Chem. B* **127**, 180–193 (2023).

817 5. Ginell, G. M. & Holehouse, A. S. An Introduction to the Stickers-and-Spacers Framework
818 as Applied to Biomolecular Condensates. in *Phase-Separated Biomolecular Condensates*
819 (eds. Zhou, H.-X., Spille, J.-H. & Banerjee, P. R.) vol. 2563 95–116 (Springer US, New York,
820 NY, 2023).

821 6. Holehouse, A. S. & Alberti, S. Molecular determinants of condensate composition.
822 *Molecular Cell* **85**, 290–308 (2025).

823 7. Su, X. *et al.* Phase separation of signaling molecules promotes T cell receptor signal
824 transduction. *Science* **352**, 595–599 (2016).

825 8. Heinkel, F. *et al.* Phase separation and clustering of an ABC transporter in
826 *Mycobacterium tuberculosis*. *Proc. Natl. Acad. Sci. U.S.A.* **116**, 16326–16331 (2019).

827 9. Tan, W. *et al.* Phase separation modulates the assembly and dynamics of a polarity-
828 related scaffold-signaling hub. *Nat Commun* **13**, 7181 (2022).

829 10. Khandelwal, N. K. & Tomasiak, T. M. Structural basis for autoinhibition by the
830 dephosphorylated regulatory domain of Ycf1. *Nat Commun* **15**, 2389 (2024).

831 11. Fiedorczuk, K. *et al.* The structures of protein kinase A in complex with CFTR:
832 Mechanisms of phosphorylation and noncatalytic activation. *Proc. Natl. Acad. Sci. U.S.A.*
833 **121**, e2409049121 (2024).

834 12. Ukleja, M. *et al.* Flotillin-mediated stabilization of unfolded proteins in bacterial
835 membrane microdomains. *Nat Commun* **15**, 5583 (2024).

836 13. López, D. & Kolter, R. Functional microdomains in bacterial membranes. *Genes Dev.* **24**,
837 1893–1902 (2010).

838 14. Gohrbandt, M. *et al.* Low membrane fluidity triggers lipid phase separation and protein
839 segregation in living bacteria. *The EMBO Journal* **41**, e109800 (2022).

840 15. Lasker, K. *et al.* The material properties of a bacterial-derived biomolecular condensate
841 tune biological function in natural and synthetic systems. *Nat Commun* **13**, 5643 (2022).

842 16. Hoang, Y. *et al.* An experimental framework to assess biomolecular condensates in
843 bacteria. *Nat Commun* **15**, 3222 (2024).

844 17. Ingólfsson, H. I. *et al.* The power of coarse graining in biomolecular simulations. *WIREs*
845 *Comput Mol Sci* **4**, 225–248 (2014).

846 18. Xiang, L., Chen, K., Yan, R., Li, W. & Xu, K. Single-molecule displacement mapping unveils
847 nanoscale heterogeneities in intracellular diffusivity. *Nat Methods* **17**, 524–530 (2020).

848 19. Śmigiel, W. M. *et al.* Protein diffusion in *Escherichia coli* cytoplasm scales with the mass
849 of the complexes and is location dependent. *Sci. Adv.* **8**, eab05387 (2022).

850 20. Linnik, D., Maslov, I., Punter, C. M. & Poolman, B. Dynamic structure of *E. coli* cytoplasm:
851 supramolecular complexes and cell aging impact spatial distribution and mobility of
852 proteins. *Commun Biol* **7**, 508 (2024).

853 21. Yan, R., Chen, K. & Xu, K. Probing Nanoscale Diffusional Heterogeneities in Cellular
854 Membranes through Multidimensional Single-Molecule and Super-Resolution
855 Microscopy. *J. Am. Chem. Soc.* **142**, 18866–18873 (2020).

856 22. Bailey, M. W., Bisicchia, P., Warren, B. T., Sherratt, D. J. & Männik, J. Evidence for
857 Divisome Localization Mechanisms Independent of the Min System and SlmA in
858 *Escherichia coli*. *PLoS Genet* **10**, e1004504 (2014).

859 23. Stacy, M. *et al.* Transient non-specific DNA binding dominates the target search of
860 bacterial DNA-binding proteins. *Molecular Cell* **81**, 1499-1514.e6 (2021).

861 24. Takamori, S., Cicuta, P., Takeuchi, S. & Di Michele, L. DNA-assisted selective electrofusion
862 (DASE) of *Escherichia coli* and giant lipid vesicles. *Nanoscale* **14**, 14255–14267 (2022).

863 25. Sun, Y., Sun, T.-L. & Huang, H. W. Physical Properties of *Escherichia coli* Spheroplast
864 Membranes. *Biophysical Journal* **107**, 2082–2090 (2014).

865 26. Culham, D. E., Romantsov, T. & Wood, J. M. Roles of K^+ , H^+ , H_2O , and $\Delta\Psi$ in Solute
866 Transport Mediated by Major Facilitator Superfamily Members ProP and LacY.
867 *Biochemistry* **47**, 8176–8185 (2008).

868 27. Mika, J. T., Van Den Bogaart, G., Veenhoff, L., Krasnikov, V. & Poolman, B. Molecular
869 sieving properties of the cytoplasm of *Escherichia coli* and consequences of osmotic
870 stress. *Molecular Microbiology* **77**, 200–207 (2010).

871 28. Elowitz, M. B., Surette, M. G., Wolf, P.-E., Stock, J. B. & Leibler, S. Protein Mobility in the
872 Cytoplasm of *Escherichia coli*. *J Bacteriol* **181**, 197–203 (1999).

873 29. Harris, R., Veretnik, S., Dewan, S., Baruch Leshem, A. & Lampel, A. Regulation of
874 enzymatic reactions by chemical composition of peptide biomolecular condensates.
875 *Commun Chem* **7**, 90 (2024).

876 30. Smirnova, I. *et al.* Oversized galactosides as a probe for conformational dynamics in LacY.
877 *Proc. Natl. Acad. Sci. U.S.A.* **115**, 4146–4151 (2018).

878 31. Mangiarotti, A. & Dimova, R. Biomolecular Condensates in Contact with Membranes.
879 *Annual Review of Biophysics* **53**, 319–341 (2024).

880 32. Renner, L. D. & Weibel, D. B. Cardiolipin microdomains localize to negatively curved
881 regions of *Escherichia coli* membranes. *Proc. Natl. Acad. Sci. U.S.A.* **108**, 6264–6269
882 (2011).

883 33. Romantsov, T. *et al.* Cardiolipin promotes polar localization of osmosensory transporter
884 *ProP* in *Escherichia coli*. *Molecular Microbiology* **64**, 1455–1465 (2007).

885 34. Santos, T. M. A., Lin, T., Rajendran, M., Anderson, S. M. & Weibel, D. B. Polar localization
886 of *E. coli* chemoreceptors requires an intact TOL – PAL complex. *Molecular
887 Microbiology* **92**, 985–1004 (2014).

888 35. Rafelski, S. M. & Theriot, J. A. Mechanism of polarization of *Listeria monocytogenes*
889 surface protein ActA. *Molecular Microbiology* **59**, 1262–1279 (2006).

890 36. De Pedro, M. A., Grünfelder, C. G. & Schwarz, H. Restricted Mobility of Cell Surface
891 Proteins in the Polar Regions of *Escherichia coli*. *J Bacteriol* **186**, 2594–2602 (2004).

892 37. Lolkema, J. S. & Poolman, B. Uncoupling in Secondary Transport Proteins. *Journal of
893 Biological Chemistry* **270**, 12670–12676 (1995).

894 38. Henderson, R. K., Fendler, K. & Poolman, B. Coupling efficiency of secondary active
895 transporters. *Current Opinion in Biotechnology* **58**, 62–71 (2019).

896 39. Mangiarotti, A. *et al.* Biomolecular condensates modulate membrane lipid packing and
897 hydration. *Nat Commun* **14**, 6081 (2023).

898 40. Juers, D. H., Matthews, B. W. & Huber, R. E. *LacZ* β -galactosidase: Structure and function
899 of an enzyme of historical and molecular biological importance. *Protein Science* **21**,
900 1792–1807 (2012).

901 41. Bickers, S. C., Sayewich, J. S. & Kanelis, V. Intrinsically disordered regions regulate the
902 activities of ATP binding cassette transporters. *Biochimica et Biophysica Acta (BBA) -*
903 *Biomembranes* **1862**, 183202 (2020).

904 42. Kassem, N., Kassem, M. M., Pedersen, S. F., Pedersen, P. A. & Kragelund, B. B. Yeast
905 recombinant production of intact human membrane proteins with long intrinsically
906 disordered intracellular regions for structural studies. *Biochimica et Biophysica Acta*
907 (*BBA*) - *Biomembranes* **1862**, 183272 (2020).

908 43. Ravindran, R. & Michnick, S. W. Biomolecular condensates as drivers of membrane
909 trafficking and remodelling. *Current Opinion in Cell Biology* **89**, 102393 (2024).

910 44. Neidhardt, F. C., Bloch, P. L. & Smith, D. F. Culture Medium for Enterobacteria. *J Bacteriol*
911 **119**, 736–747 (1974).

912 45. Yan, R., Chen, K. & Xu, K. Probing Nanoscale Diffusional Heterogeneities in Cellular
913 Membranes through Multidimensional Single-Molecule and Super-Resolution
914 Microscopy. *J. Am. Chem. Soc.* **142**, 18866–18873 (2020).

915 46. MembraneEnzymology. MembraneEnzymology/smdm: SMdM analysis in *Escherichia coli*
916 cytoplasm. Zenodo <https://doi.org/10.5281/ZENODO.5911836> (2022).

917 47. MembraneEnzymology. MembraneEnzymology/PALM_Reconstruction: PALM
918 Reconstruction v1.0. Zenodo <https://doi.org/10.5281/ZENODO.14334015> (2024).

919 48. McDONALD, K. L. & Webb, R. I. Freeze substitution in 3 hours or less: FREEZE
920 SUBSTITUTION IN 3 HOURS OR LESS. *Journal of Microscopy* **243**, 227–233 (2011).

921 49. Abramson, J. *et al.* Accurate structure prediction of biomolecular interactions with
922 AlphaFold 3. *Nature* **630**, 493–500 (2024).

923 50. Abraham, M. *et al.* GROMACS 2024.3 Manual. (2024) doi:10.5281/ZENODO.13457083.

924 51. Abraham, M. J. *et al.* GROMACS: High performance molecular simulations through multi-
925 level parallelism from laptops to supercomputers. *SoftwareX* **1–2**, 19–25 (2015).

926 52. Souza, P. C. T. *et al.* Martini 3: a general purpose force field for coarse-grained molecular
927 dynamics. *Nat Methods* **18**, 382–388 (2021).

928 53. Kroon, P. *et al.* Martinize2 and Vermouth: Unified Framework for Topology Generation.
929 Preprint at <https://doi.org/10.7554/eLife.90627.2> (2024).

930 54. Drozdetskiy, A., Cole, C., Procter, J. & Barton, G. J. JPred4: a protein secondary structure
931 prediction server. *Nucleic Acids Res* **43**, W389–W394 (2015).

932 55. Lasker, K. *et al.* The material properties of a bacterial-derived biomolecular condensate
933 tune biological function in natural and synthetic systems. *Nat Commun* **13**, 5643 (2022).

934 56. Ruff, K. M. & Pappu, R. V. AlphaFold and Implications for Intrinsically Disordered
935 Proteins. *Journal of Molecular Biology* **433**, 167208 (2021).

936 57. Wang, L., Brasnett, C., Borges-Araújo, L., Souza, P. C. T. & Marrink, S. J. Martini3-IDP:
937 improved Martini 3 force field for disordered proteins. *Nat Commun* **16**, 2874 (2025).

938 58. Westendorp, M. S. S., Stevens, J. A., Bruininks, B. M. H. & Marrink, S.-J. Bentopy: building
939 molecular dynamics simulations with cellular complexity and scale. Zenodo
940 <https://doi.org/10.5281/ZENODO.13818758> (2024).

941 59. Wassenaar, T. A., Ingólfsson, H. I., Böckmann, R. A., Tieleman, D. P. & Marrink, S. J.
942 Computational Lipidomics with *insane* : A Versatile Tool for Generating Custom
943 Membranes for Molecular Simulations. *J. Chem. Theory Comput.* **11**, 2144–2155 (2015).

944 60. Pogozheva, I. D. *et al.* Comparative Molecular Dynamics Simulation Studies of Realistic
945 Eukaryotic, Prokaryotic, and Archaeal Membranes. *J. Chem. Inf. Model.* **62**, 1036–1051
946 (2022).

947 61. De Jong, D. H., Baoukina, S., Ingólfsson, H. I. & Marrink, S. J. Martini straight: Boosting
948 performance using a shorter cutoff and GPUs. *Computer Physics Communications* **199**,
949 1–7 (2016).

950 62. Kim, H., Fábián, B. & Hummer, G. Neighbor List Artifacts in Molecular Dynamics
951 Simulations. *J. Chem. Theory Comput.* **19**, 8919–8929 (2023).

952 63. Gowers, R. *et al.* MDAnalysis: A Python Package for the Rapid Analysis of Molecular
953 Dynamics Simulations. in 98–105 (Austin, Texas, 2016). doi:10.25080/Majora-629e541a-
954 00e.

955 64. Michaud-Agrawal, N., Denning, E. J., Woolf, T. B. & Beckstein, O. MDAnalysis: A toolkit
956 for the analysis of molecular dynamics simulations. *J Comput Chem* **32**, 2319–2327
957 (2011).

958 65. Humphrey, W., Dalke, A. & Schulten, K. VMD: Visual molecular dynamics. *Journal of
959 Molecular Graphics* **14**, 33–38 (1996).

960 66. Hunter, J. D. Matplotlib: A 2D Graphics Environment. *Comput. Sci. Eng.* **9**, 90–95 (2007).

961 67. Baba, T. *et al.* Construction of *Escherichia coli* K-12 in-frame, single-gene knockout
962 mutants: the Keio collection. *Molecular Systems Biology* **2**, 2006.0008 (2006).

963 68. Hanahan, D. Studies on transformation of *Escherichia coli* with plasmids. *Journal of
964 Molecular Biology* **166**, 557–580 (1983).

965

966

Table 1. List of *E. coli* strain used in the work.

Name	Plasmid	Purpose	Source / Reference
BW25113	-	Expression of genes, protein production	67
DH5 α	-	Storage of plasmids	68
BW25113 $\Delta lacY$	-	Deletion of lactose permease gene	67
LY177	-	MG1655 derivative with inducible nucleoid degradation	23
DH5 α pACYC LacY	pACYC_LacY-mEos3.2	Source of <i>lacY</i> gene and pACYC vector	27
DH5 α PopZ-eGFP	pMA-RQ_popZ-mRuby	Source of <i>popZ</i> and <i>mRuby</i> genes	20
DH5 α mEos3.2	pBAD_mEos3.2	Source of <i>mEos3.2</i> gene and pBAD vector	19
BW25113 LacY ^{mEos}	pBAD_LacY-mEos3.2	Expression of LacY-mEos3.2 fusion for visualization	This work
BW25113 LacY ^{mEos} -Pop	pBAD_LacY-mEos3.2-PopTag	Expression of LacY-mEos3.2 fusion for visualization	This work
BW25113 $\Delta lacY$ LacY ^{mEos}	pBAD_LacY-mEos3.2	Expression of LacY for lactose uptake experiments	This work
BW25113 $\Delta lacY$ LacY ^{mEos} -Pop	pBAD_LacY-mEos3.2-PopTag	Expression of LacY-PopTag for lactose uptake experiments	This work
LY177 LacY ^{mEos}	pSN1	LacY-mEos3.2 fusion visualization in cells with degraded nucleoid	This work
	pACYC_LacY-mEos3.2		
LY177 LacY ^{mEos} -Pop	pSN1	LacY-mEos3.2-PopTag fusion for visualization of cells with degraded nucleoid	This work
	pACYC_LacY-mEos3.2-PopTag		
BW25113 LacY ^{mEos} -LacZ ^{mRuby}	pBAD_LacY-mEos3.2	Expression of LacY-mEos3.2 and LacZ-mRuby fusions for visualization	This work
	pACYC_LacZ-mRuby		
BW25113 LacY ^{mEos} -Pop-LacZ ^{mRuby}	pBAD_LacY-mEos3.2-PopTag	Expression of LacY-mEos3.2-PopTag and LacZ-mRuby fusions for visualization	This work
	pACYC_LacZ-mRuby		
BW25113 LacY ^{mEos} -LacZ ^{mRuby} -Pop	pBAD_LacY-mEos3.2-PopTag	Expression of LacY-mEos3.2 and LacZ-mRuby-PopTag fusions for visualization	This work
	pACYC_LacZ-mRuby-PopTag		
BW25113 LacY ^{mEos} -Pop-LacZ ^{mRuby} -Pop	pBAD_LacY-mEos3.2-PopTag	Expression of LacY-mEos3.2-PopTag and LacZ-mRuby-PopTag fusions for visualization	This work
	pACYC_LacZ-mRuby-PopTag		
BW25113 $\Delta lacY$ LacY-LacZ	pBAD_LacY	Expression of LacY and LacZ proteins for functional tests	This work
	pACYC_LacZ		
BW25113 $\Delta lacY$ LacY ^{Pop} -LacZ	pBAD_LacY-PopTag	Expression of LacY-PopTag and LacZ proteins for activity assays	This work
	pACYC_LacZ		
BW25113 $\Delta lacY$ LacY-LacZ ^{Pop}	pBAD_LacY	Expression of LacY and LacZ-PopTag proteins for activity assays	This work
	pACYC_LacZ-PopTag		
BW25113 $\Delta lacY$ LacY ^{Pop} -LacZ ^{Pop}	pBAD_LacY-PopTag	Expression of LacY-PopTag and LacZ-PopTag proteins for activity assays	This work
	pACYC_LacZ-PopTag		

967

Supplementary Files

This is a list of supplementary files associated with this preprint. Click to download.

- [SupplementarydataStructuralandfunctionalimplicationsofinvivophasesseparationofmembraneproteininEscherichiacoli.pdf](#)